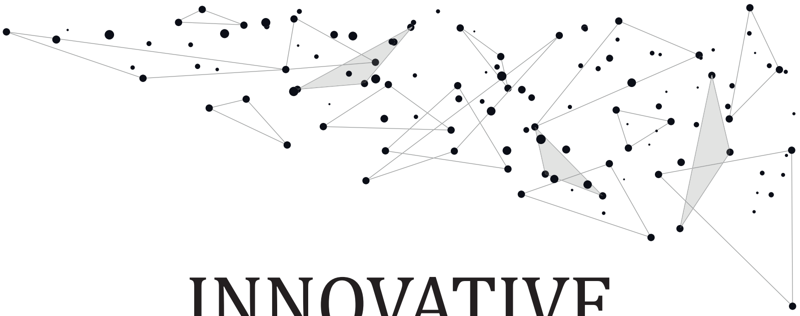

INNOVATIVE APPROACHES IN SCIENCE AND MATHEMATICS

GECE AKADEMİ

Kitap Adı : **Innovative Approaches in Science and Mathematics**
İmtiyaz Sahibi/Publisher : Gece Kitaplığı
Genel Yayın Yönetmeni/Editor in Chief : Doç. Dr. Atilla ATİK
Proje Koordinatörü/Project Coordinator : Ethem BİLİCİ
Kapak&İç Tasarım/Cover&Interior Design : Özge ERGENEL
Sosyal Medya/Social Media : Arzu ÇUHACIOĞLU
Yayına Hazırlama : Gece Akademi Dizgi Birimi

Sertifika/Certificate No : 34559
ISBN : 978-605-288-805-6

Editör/Editors

Prof. Dr. Hüsniye AKA SAĞLIKER
Doç. Dr. Sadık ÇOĞAL
Doç. Dr. Seçkin KÖROĞLU

GECE AKADEMİ

Gece Publishing
ABD Adres/ USA Address: 387 Park Avenue South, 5th Floor, New York, 10016, USA
Telefon/Phone: +1 347 355 10 70

Gece Kitaplığı
Türkiye Adres/Turkey Address: Kızılay Mah. Fevzi Çakmak 1. Sokak Ümit Apt. No: 22/A Çankaya/Ankara/TR
Telefon/Phone: +90 312 431 34 84 - +90 555 888 24 26

web: www.gecekitapligi.com —www.gecekitap.com
e-mail: geceakademi@gmail.com

INNOVATIVE APPROACHES IN SCIENCE AND MATHEMATICS

GECE
AKADEMİ

CONTENTS

CHAPTER 1

SOME EXAMPLES FOR IRON PHTHALOCYANINES AS EFFICIENT CATALYSTS

Barbaros AKKURT[1], Altuğ Mert SEVIM[2]

INTRODUCTION

Phthalocyanines are completely aromatic molecules, having eight nitrogen atoms connecting four indole fragments to each other. They are resistant to heat, acids, bases, and reducing agents. Synthetic methods of phthalocyanines are different for different substituted ones. There are peripheral tetrasubstitution, peripheral octasubstitution, and non-peripheral tetrasubstitution and non-peripheral octasubstution. Substitution makes phthalocyanines more soluble in common organic solvents, which makes them more useable in certain applications.

This book chapter deals with iron phthalocyanines and their applications between years 2000 and 2018. We have found out that iron(II) or iron(III) phthalocyanines have been used as very effective catalysts for oxidation reactions, in which the yields are sometimes quantitative in oxygen reduction reaction (orr), a catalyst in fuel cells like DFMC, microbial fuel cells, PEMFCs, chemically regenerative redox fuel cells, and alkaline direct ethanol fuel cells. In addition, they have been used as catalysts in several organic transformations like olefination of aldehydes, aerobic hydration and C-H hydroxylation, synthesis of 2-amino-1-phenylethanols from olefins, synthesis of spiroacridines, catalytic transfer hydrogenation of simple aldehydes and ketones, iron-catalyzed regioselective synthesis of 3-arylindoles, synthesis of sulfones from sulfonylhydrazones, and oxygen reduction reaction of iron phthalocyanines with bound oxygen molecule.

We hope that the readers enjoy this treatise about iron phthalocyanines. Since iron phthalocyanines, both unsubstituted and substituted, are used in very diverse areas, this diversity makes researchers all around the world study with these catalytic molecules and the authors believe that many doors will be opened both molecular design and catalytic applications.

---

[1] Lecturer, PhD, Istanbul Technical University, Faculty of Science and Letters, Department of Chemistry, 34469 Maslak-Sariyer/Istanbul. E-mail: akkurtb@itu.edu.tr.

[2] Assoc. Prof. Dr., Istanbul Technical University, Faculty of Science and Letters, Department of Chemistry, 34469 Maslak-Sariyer/Istanbul. E-mail: sevim@itu.edu.tr.

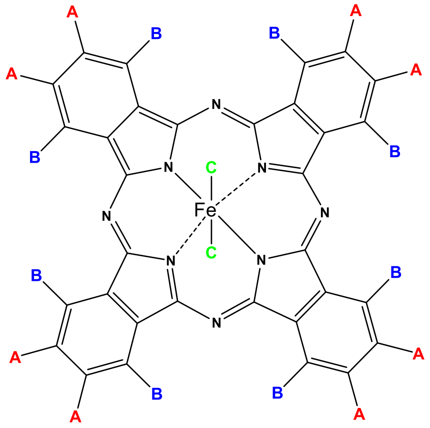

A= Peripheral Sites
B= Non-peripheral Sites
C= Axial Sites

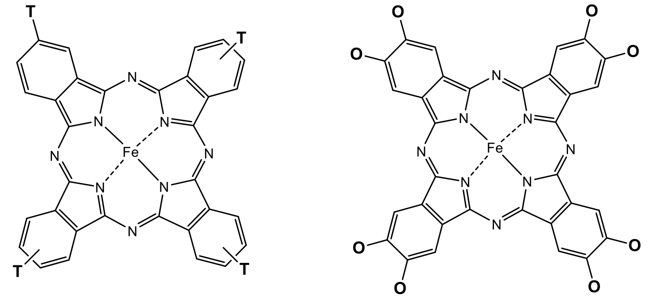

Tetra-substituted iron phthalocyanines

Octa-substituted iron phthalocyanines

Scheme 1: Phthalocyanines with tetra- and octa- substitutions

Some Examples for Iron Phthalocyanines as Catalysts

Oxidation reactions

Oxidation of cyclohexane

In a study by Grootboom and Nyokong in 2002, they studied with perchlorophthalocyaninatoiron(II) and tetrasulfophthalocyaninatoiron(II) were used to oxidize cyclohexane with a mixture of three oxidants, namely tert-butylhydroperoxide, m-chloroperoxybenzoic acid, and hydrogen peroxide. Some solvent mixtures were used to include organics in the reaction medium. Cyclohexanone, cyclohexanol, and cyclohexanediol were observed as the products. Tert-butylhydroperoxide was the best oxidant because it gives minimal damage to the catalyst and the selectivities were higher. The iron(II) phthalocyanine was observed to oxidize to iron(III) phthalocyanine during the reaction. It is interesting to note that with perchlorophthalocyaninatoiron(II), no cyclohexanediol was produced (Grootboom & Nyokong 2002:113).

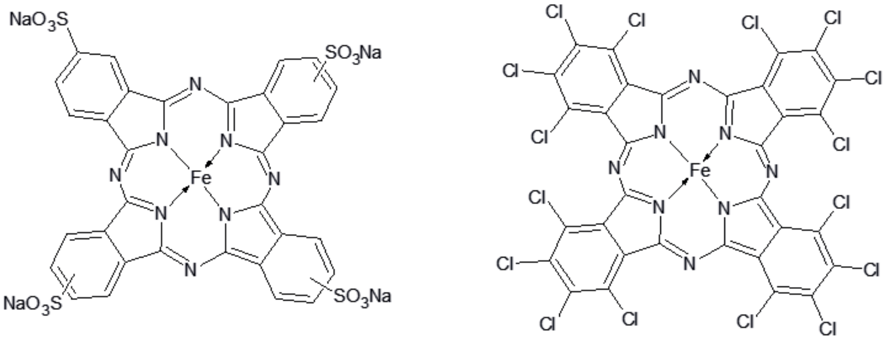

Figure 1. Chemical structures of tetrasulfophthalocyaninatoiron(II) on the left and perchlorophthalocyaninatoiron(II) on the right.

Electrooxidation reactions

Electrooxidation of 2-mercaptoethanol was studied by Aguirre et al (2002), by including some substituted and unsubstituted iron(II) phthalocyanines as electrocatalysts. The catalysts were pre-adsorbed on pyrolytic graphite. They studied methoxy, hydrogen (unsubstituted Pc), carboxy, sulfonate, and chloro substituted phthalocyanines. Redox processes of iron(II) to iron(I) and iron(III) to iron(II) were shifted to more positive potentials with carboxy, sulfonate, and chloro substitutients and to more negative potential with methoxy as compared to the unsubstituted phthalocyanine. The electrocatalytic activities were presented in the following order: $Cl_{16}FePc < (SO_3)_4FePc < (COO)_4FePc < FePc < (OMe)_8FePc$ (Aguirre, Isaacs, Armijo, Basáez, & Zagal, 2002:356).

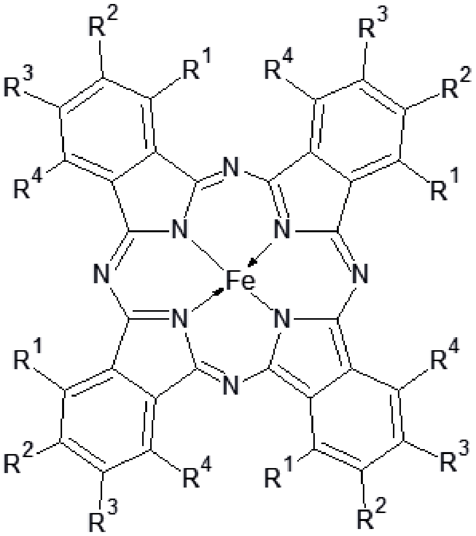

Figure 2. Chemical structures of the phthalocyanines used.

FePc: $R^1 = R^2 = R^3 = R^4 = H$

(MeO)$_8$FePc: $R^1 = R^4 = H, R^2 = R^3 = OMe$

Cl$_{16}$FePc: $R^1 = R^2 = R^3 = R^4 = Cl$

$(SO_3)_4FePc$: R^2 (R^3) = SO_3^-, $R^1 = R^4$ = H

$(COO)_4FePc$: R^2 (R^3) = COO^-, $R^1 = R^4$ = H.

Oxidative cyanation of tertiary amines

Tertiary amines are reportedly cyanated in the presence of tetrasulfoiron(II)phthalocyanine by anchoring to a polymeric amine scaffold. The products were α-aminonitriles and yields and selectivities were high. The oxidant was hydrogen peroxide and the cyanation agent was sodium cyanide. There was no metal leaching, which is considered as an advantage in this method (Singhal, Jain, & Sain, 2010).

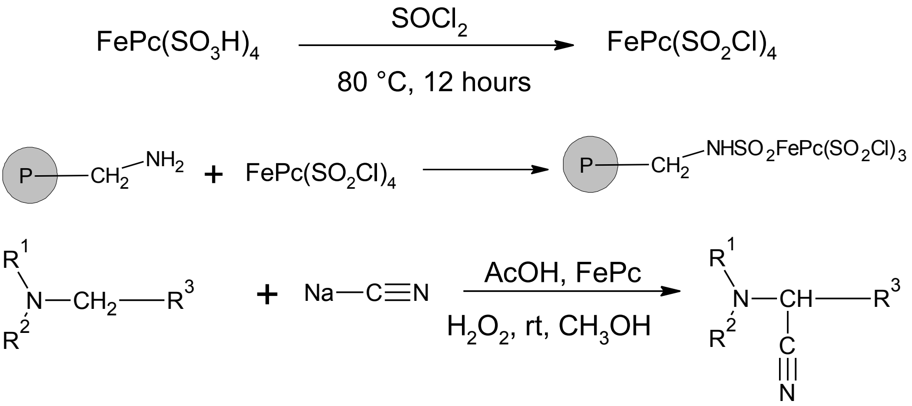

Figure 3. Oxidative cyanation of tertiary amines.

As a successful example, N,N-dimethylaniline was reacted with tetrachlorosulfonyliron(II) phthalocyanine and polymer-anchored scaffold for 2.5 hours and the product was N-methyl-N-cyanomethylaniline and the conversion was 98% while the yield was 92% (Singhal, Jain & Sain, 2010:1338).

Catalytic oxidation in the presence of a phthalocyanine

2-methyl-1-naphthol was catalytically oxidized, where the catalyst was iron phthalocyanine, to yield 2-methyl-1,4-naphthoquinone (also known as vitamin K). The phthalocyanine contained four sulfo groups on the periphery. Amino-modified silica was used to anchor the catalyst by utilizing a new one-pot reaction, where triphenylphosphine triflate was the activator. Tert-butylhydroperoxide was the oxidant in the study. The selectivity and conversion of the synthesis of Vitamin K_3 was 59% and 96% respectively, and only 0.5 mol% of the catalyst was used. The mechanism of oxidation indicates that it was not of radical-based (Zalomaeva, Kholdeeva, & Sorokin, 2007).

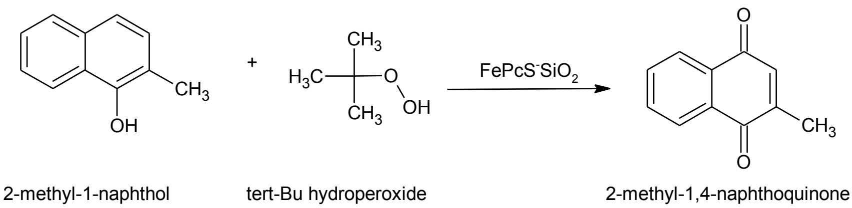

Figure 4. 2-Methyl-1-naphthol was reacted with tert-butylhydroperoxide to yield 2-methyl-1,4-naphthoquinone.

Primary or secondary benzylic alcohols' oxidation

Geraskin et al (2008) studied the oxidation of primary or secondary benzylic alcohols, in which the oxidants were iodoxybenzoic acid (IBX esters) and 2-iodylphenol ethers. Iodosylbenzene was not used because of its explosive nature. When the oxidant was isopropyl IBX ester, the catalyst was μ-oxo(tetra-tert-butylphthalocyaninato)iron(III) dissolved in dichloromethane (at 0.1% equiv) and the reaction time was 0.5-2 hours, yielding the related carbonyl compounds. The conversion was 100% and preparative yields at 91-95% were achieved with column chromatography (Geraskin, Luedtke, Neu, Nemykin, & Zhdankin, 2008: 7410).

Oxidation of alkyl substituted phenols

2,3,6-Trimethylphenol and 2-methyl-1-naphthol were oxidized to yield 2,3,5-trimethylbenzoquinone, (a precursor of vitamin E), and 2-methylnaphthoquinone (vitamin K_3). The oxidant was tert-butylhydroperoxide and the catalyst was silica-supported iron tetrasulfophthalocyanine in the form of μ-oxo dimer. The authors reported that there was two successive electron transfer involved (Zalomaeva, Ivanchikova, Kholdeeva, & Sorokin, 2009: 1031).

Methane oxidation

Nitrogen-bridged diiron phthalocyanine ($[PcFe^{+3.5}NFe^{+3.5}Pc]^0$) is quite powerful to oxidize methane with a two-electron process under conditions that are near-ambient. After a two-electron oxidation, the iron phthalocyanine turns $[PcFe^{(4)}NFe^{(4)}Pc]^+ PF_6$ and $[PcFe^{(4)}NFe^{(4)}(Pc^{\bullet+})]^{2+}Br_2$ as intermediary products in the catalytic cycle (Kudrik et al., 2012: 43).

Oxidation of methane with N-bridged FePc

Methane was oxidized with hydrogen peroxide in water medium and a μ-nitridoiron phthalocyanine complex was used as the catalyst, grafted on silica. Methyl hydroperoxide was the main reaction product (Forde et al., 2012: 177).

Catalytic Aerobic Oxidation of Arylhydrazides

In a study by Taniguchi *et al.* in 2015, a practical method was recommended for the preparation of 2-arylazocarboxylates and their derivatives from the corresponding 2-arylhydrazinecarboxylates. The oxidant was air and the catalyst was iron phthalocyanine, which is inexpensive and non-toxic. Since the reaction system is economically and environmentally benign, it is a good model of practical synthesis (Hashimoto, Hirose, & Taniguchi, 2014: 3346).

Aerobic alcohol oxidation

Mahyari and Shaabani (2014) have successfully developed an iron phthalocyanine catalyst which is highly active and covalently supported on graphene oxide nanosheets. Primary and secondary alcohols were oxidized in the presence of this new heterogeneous catalyst for the synthesis of corresponding aldehydes or ketones, by molecular oxygen as oxidant, under optimal and environmentally-benign reaction conditions with high conversions in up to 97% yield. Moreover, without significant loss of activity and selectivity, the catalyst can be reused several times (Mahyari & Shaabani, 2014: 524).

Oxidation of cyclohexene with Co(II)- and Fe(II)-based phthalocyanines

The substituted Co(II) and Fe(II) phthalocyanines as possible catalysts were prepared by Saka and Biyiklioglu (2013). Cyclohexene was used as the substrate, while tert-butylhydroperoxide, m-chloroperoxybenzoic acid, aerobic oxygen, hydrogen peroxide, and potassium peroxomonosulfate were employed as oxidants. Iron phthalocyanine was superior to the cobalt phthalocyanine in terms of product yields and selectivity. The major product was 2-cyclohexene-1-ol. cyclohexene oxide and 2-cyclohexene-1-one were minor products. When the oxidants were investigated, it was found that TBHP was a better oxidant and when reacted with cyclohexene and metal phthalocyanines, iron phthalocyanine yielded 98% catalytic activity compared than 87% for cobalt phthalocyanine. (Saka & Bıyıklıoğlu, 2013: 50).

Oxygen reduction reaction (orr)

Influence of alpha- or beta-phases on orr

The researchers found by XRD that FePc was under alpha phase under normal conditions while it was under beta phase when heated. They compared the phases of FePc towards orr. Alpha phase was 100 mV lower than that of beta phase. Electrochemical quartz crystal microbalance measurements showed that alpha phase formed PcFe-O-FePc structure against beta phase, 700 mV less versus RHE. When orr was carried out at the alpha phased FePc, there were two reduction waves. The first wave was about the formation of the dimeric structure while the second wave was related to the monomeric FePc's oxygen adsorption and reduction (Baranton, Coutanceau, Garnier, & Léger, 2006: 100)

Electrocatalytic performance

Baranton *et al.* dispersed iron(II) over a carbon substrate with high surface area and the electrocatalytic behavior was investigated. In an oxygen-saturated solution, the polarization curve for the FePc-C system in methanol was compared with the Pt catalyst. According to the results, FePc-C is better with an intolerance to methanol than Pt/C at low overpotentials. This means that FePc-C catalyst could be used as a cathodic one in low working temperature fuel cells. The new catalyst has problems in acidic medium in that it is not stable long-term, which was remedied with a gas diffusion electrode for at least 24 hours. Kinetic parameters for the orr of the iron catalyst are similar to that of the platinum catalyst. Rotating disc electrode experiments show that the number of total electrons exchanged is almost 4 (Baranton, Coutanceau, Roux, Hahn, & Léger, 2005: 223).

Fe/N/C electrocatalysts in the oxygen reduction reaction

It has been debated about cobalt(II) phthalocyanine catalyzing the orr, and many researchers tried to substitute these phthalocyanines and porphyrins for platinum, a very expensive element. The researchers studied carbon-supported FePc pyrolyzed at 800 °C, in the presence of azide in acidic, neutral and basic environments. The presence of azide helped greater orr activity in neutral electrolyte, whereas no activity was observed in acidic or basic environments (Oberst, Thorum, & Gewirth, 2012: 25257).

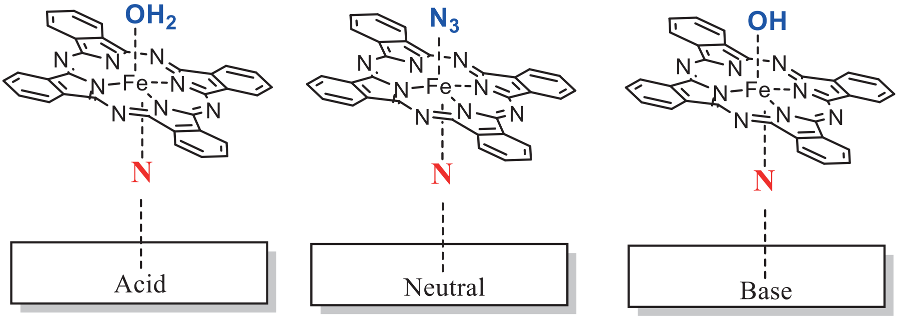

Figure 5: Carbon supported phthalocyanines in different environments.

Pt-free FePc on graphene support in oxygen reduction reaction

If fuel cells are planned to be employed at large scale, then one must accept that low-cost, efficient, and stable electrocatalysts must replace the noble metal-based ones. The authors found when iron phthalocyanine was supported on chemically reduced graphene via π-π interactions, the catalyst is able to behave as if a noble metal-based catalyst was used, and the operational stability was long, and tolerance to methanol crossover was better. Poisoning from CO also improved. The catalyst is able to follow four electron reduction from oxygen to water (Jiang et al., 2013: 1263).

In situ Scanning Tunneling Microscopy used in Single-Molecule Imaging of Oxygen Reduction Reaction

Iron-phthalocyanine (FePc)-catalyzed orr was investigated with in situ electrochemical scanning tunneling microscopy (ECSTM) to study the catalytic role of the FePc molecules. CV results showed that Au(111) electrode modified with FePc- had a significant electrocatalytic activity for the reduction of oxygen (Gu, Cai, Wang, & Wan, 2016: 8746).

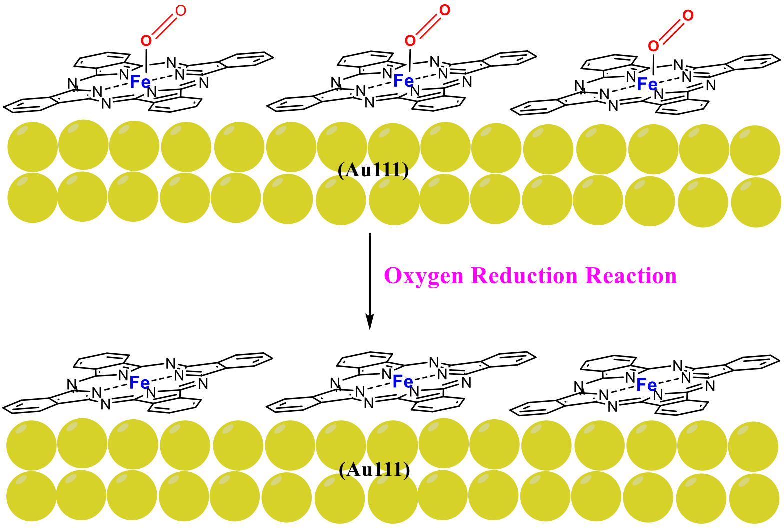

Figure 6. Orr catalyzed by FePc.

Binuclear iron phthalocyanine with high crystallinity

When binuclear iron phthalocyanine was coated onto multiwalled carbon nanotubes, it could be used as an orr catalyst stable for 14 h to give the current. TEM studies showed that the crystalline phthalocyanine was uniformly coated on the carbon nanotubes with 20 nm thickness. The orr was not disrupted in the presence of methanol; it was not oxidized. A direct 4-electron catalysis from oxygen to water was achieved (Hu, Xia, Zhang, & Zhang, 2013).

Uses in Fuel Cells

Use in Direct Methanol Fuel Cells (DMFC)

In the research by Baranton *et al.*(2005), FePc cathodes were prepared by dispersing FePc supported on C or by electropolymerizing aniline in the presence of FeTsPc as catalyst. The new systems were compared to the conventional Pt/C, while standard electrode cell conditions and DMFC system was used. When FeTsPc was dispersed on PAni (polyaniline) film, the orr was enhanced greatly. The ratio of no of Pt atoms / no of FeTsPc per cm^2 should be close to 100 if one wants to be optimistic about the development of polymer-FeTsPc electrodes. With DMFC cells, which do not contain platinum-based electrodes, the researches should be conducted around new electron-conductive polymers (they should be stable under oxidative conditions) and they should have high doping capacity (Baranton, Coutanceau, Léger, Roux, & Capron, 2005: 517).

Use of FePc in Microbial Fuel Cells

The authors discussed the performance of the catalysts of oxygen reduction, namely platinum, pyrolyzed FePc (pyr-FePc) and cobalt tetramethoxyphenylporphyrin (pyr-CoTMPP) in microbial fuel cells. The chemical and physical conditions severely affect the thermodynamics and kinetics of the electrocatalytic orr. Neutrality of pH, low buffer capacities, and low ionizations affect the cathodic performance and the limitation of the fuel cell in a strong manner (Zhao et al., 2006: 5193).

Polymer Electrolyte Membrane Fuel Cell Catalysts (PEMFCs)

Li and coworkers (2010) designed and prepared a highly durable Fe-SPc orr catalyst for PEMFCs. The inspiration from natural oxygen activation catalysts enabled them to prepare the Fe-SPc structure. The preparation did not involve any pyrolytic method. The Fe-SPc was compared to commercially obtained FePc and the current density of FeSPc was 7.4 times higher than that of FePc after 100 cycles. The reason was that there were electron-donating groups at the peripheral positions. Active site isolation is maintained by high degree of steric hindrance . Therefore Fe-SPc is a promising alternative for orr electrocatalyst in the PEMFCs (Li, Yu, Higgins, Llanos, & Chen, 2010: 17056).

Use in the degradation of microbial fuel cell and catalytic oxidation reactor, with FePc as catalyst

A microbial fuel cell (MFC) and a catalytic oxidation reactor (COR) were used in which H_2O_2 was obtained at the MFC cathode and residual dissolved oxygen could both be used as oxidants, with iron phthalocyanine-based catalyst, for Congo red degradation. The performance was high and more than 90% of Congo Red was degraded after 72 hours in neutral solution. The catalyst was still active after 33 cycles. LC–MS analysis showed that Congo red was decomposed into less toxic and more biodegradable compounds like malonic acid and maleic acid. This MFC-COR system can be a promising alternative for the removal of refractory and biodegradable pollutant (Yuan, Li, Lv, Zhang, & Yang, 2017: 118).

Performance in an Alkaline Direct Ethanol Fuel Cell of Oxygen Reduction Reaction

Using Fe(II)-phthalocyanine, an Fe-N-C non-noble metal (NNM) catalyst for orr was prepared in which hard templating method was used. The results showed that the orr occurs mainly following the direct 4 e^- reduction to OH^-, and that the prepared catalyst is highly tolerant to ethanol and its stability is promising (Osmieri, Escudero-Cid, Monteverde Videla, Ocón, & Specchia, 2018: 226).

Uses in organic reactions

Olefination of aldehydes

In a publication appeared in 2004, aliphatic and aromatic aldehydes were converted into their olefins with yields near excellent. The reaction involved ethyldiazoacetate and as a catalyst, FePc (no substituents) was used and triphenylphosphine, as the reducing agent, was added into the medium. The simplified reaction is RCHO + $N_2CHCOOEt$ + Ph_3P --> RCH=CHCOOEt + Ph_3PO and the solvent was toluene and nitrogen atmosphere was maintained throughout the reaction. As an example, when starting from p-nitrobenzaldehyde one obtains p-nitrophenylethenylcarboxylic acid ethyl ester in 96% yield by reacting for 2 hours. The yields were excellent and high *trans* selectivity was observed. The oxygen of the aldehyde is transferred to triphenylphosphine and this is the evidence of the reducing action of the latter. Similarly, iron(II) phthalocyanine is crucial to the reaction; its absence blocks the reaction from being completed (Sharma, Jain, & Sain, 2004: 141).

Hydration and C-H Hydroxylation in Aerobic Medium

In a study by Hashimoto *et al.* in 2014, a novel 1,4-hydroxylation reaction of aliphatic alkenes was developed involving C(sp^3)-H oxygenation. This reaction allowed all types of C(sp^3)H bonds (primary, secondary, tertiary centers) to yield various 1,4- diols from simple alkenes, employing nontoxic and inexpensive reagents under mild conditions. O$_2$ was the source for the two oxygen atoms of the final product. Iron(II) phthalocyanine was used as a catalyst at 10 mol% (Hashimoto, Hirose, & Taniguchi, 2014: 2730).

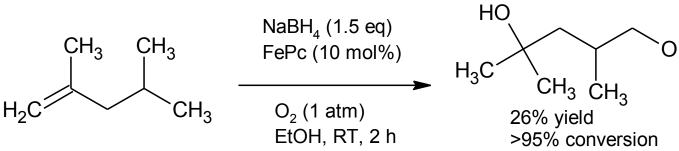

Figure 7. Hydroxylation of alkenes.

Direct Catalytic Synthesis of Unprotected 2-Amino-1-Phenylethanols from Alkenes

Legnani and Morandi (2016) reported the first exceptionally simple and inexpensive aminohydroxylation of unprotected amino alcohols from simple alkenes; the yields were good and regioselectivity was perfect. The process conditions were mild and iron phthalocyanine is a commercially available and inexpensive. This new catalytic method was applied in the expedient synthesis of bioactive molecules and could be extended to aminoetherification (Legnani & Morandi, 2016: 2248).

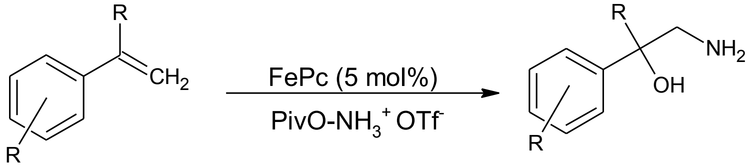

Figure 8. An aminohydroxylation example with iron(II) phthalocyanine.

Diarylamines' Iron-Catalyzed Oxidative C-C and N-N Coupling and Synthesis of Spiroacridines

Diarylamines underwent iron phthalocyanine-catalyzed intermolecular oxidative coupling, to yield 2,2'-bis(arylamino)biaryls, tetraarylhydrazines, and 5,6-dihydrobenzo[c]cinnolines and the catalyst was hexadecafluoroiron phthalocyanine. The conditions of C-C or N-N formation was mild, and some acids and bases can be used to control the reaction (methanesulfonic acid, Hünig's base, acetic acid, etc.). (Fritsche, Theumer, Kataeva, & Knölker, 2017: 549).

Catalytic transfer hydrogenation of simple aldehydes and ketones

In another study by Bata et al (2015), catalytic transfer hydrogenation (CTH) of various carbonyl products was studied using FePc as the catalyst, in order to substitute for very expensive metals iridium, rhodium, and ruthenium with an easily available and cheaper metal. According to their results, the FePc complex is well-suited for the CTH reactions of various aldehydes and ketones. To summarize, CTH of differently substituted aldehydes and ketones was studied, using FePc catalyst and propan-2-ol as the hydrogen source. This catalytic system's performance was moderate to excellent for simple aldehydes and reasonable for ketones. It was shown that the heterogeneous catalyst was easy to separate, and it was then successfully used in repeated runs (Bata, Notheisz, Kluson, & Zsigmond, 2015: 45).

Iron-Catalyzed Regioselective Synthesis of 3-Arylindoles

3-Arylindoles were produced from FePc as catalyst and nitrosoarenes and alkynes as reactants, as reported by Yin et al (2017). The reductant was carbon monoxide and many nitrosoarenes and alkynes were transformed into their indoles with good yields, and the tolerance to functional groups was excellent. The reductant was not only carbon dioxide, but also isopropanol was used as well (Yin, Wang, & Wu, 2017: 6689).

Synthesis of sulfones from sulfonylhydrazones

In this study, sulfonylhydrazones catalyzed by iron(III) phthalocyanine chloride were used to synthesize sulfone compounds. Many substrates could be used, mild conditions were exercised, the reactants are readily available, and reaction yields were good and even high. To synthesize new sulfones, this method is new, simple enough, and promising to obtain functionalized sulfones in sulfur chemistry (J.-L. Zhao et al., 2016: 2375).

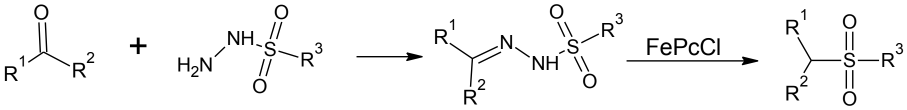

Figure 9. An example of sulfone synthesis in the presence of an iron phthalocyanine.

REFERENCES

1. AGUIRRE, M. J., ISAACS, M., ARMIJO, F., BASÁEZ, L., & ZAGAL, J. H. (2002), "Effect of the Substituents on the Ligand of Iron Phthalocyanines Adsorbed on Graphite Electrodes on Their Activity for the Electrooxidation of 2-Mercaptoethanol", Electroanalysis, Vol. 14, Issue 5, pp. 356–362.
2. BARANTON, S., COUTANCEAU, C., GARNIER, E., & LÉGER, J.-M. (2006), "How does α-FePc catalysts dispersed onto high specific surface carbon support work towards oxygen reduction reaction (orr)?", Journal of Electroanalytical Chemistry, Vol. 590, Issue 1, pp. 100–110.
3. BARANTON, S., COUTANCEAU, C., LÉGER, J.-M., ROUX, C., & CAPRON, P. (2005), "Alternative cathodes based on iron phthalocyanine catalysts for mini- or mi-

cro-DMFC working at room temperature", Electrochimica Acta, Vol. 51, Issue 3, pp. 517–525. https://doi.org/10.1016/j.electacta.2005.05.010

4. BARANTON, S., COUTANCEAU, C., ROUX, C., HAHN, F., & LÉGER, J.-M. (2005), "Oxygen reduction reaction in acid medium at iron phthalocyanine dispersed on high surface area carbon substrate: tolerance to methanol, stability and kinetics", Journal of Electroanalytical Chemistry, Vol. 577, Issue 2, pp. 223–234.
5. BATA, Péter, NOTHEISZ, Ferenc, KLUSON, Peter, & ZSIGMOND, Ágnes, (2015), ”Iron phthalocyanine as new efficient catalyst for catalytic transfer hydrogenation of simple aldehydes and ketones: Catalytic transfer hydrogenation of carbonyl functionality", Applied Organometallic Chemistry, Vol. 29, Issue 1, pp. 45–49.
6. FORDE, Michael M., GRAZIA, Bezzu C., ARMSTRONG, Robert, JENKINS, Robert L., RAHIM, Mohammed Hasbi A., CARLEY, Albert F.,DIMITRATOS, Nikolaos, LOPEZ-SANCHEZ, Jose A., TAYLOR, Stuart H., MCKEOWN Neil B., HUTCHINGS, Graham John. (2012), "Methane oxidation using silica-supported N-bridged diiron phthalocyanine catalyst", Journal of Catalysis, Vol. 290, pp. 177–185.
7. FRITSCHE, Raphael F., THEUMER, Gabriele, KATAEVA, Olga, & KNÖLKER, Hans-Joachim, (2017), "Iron-Catalyzed Oxidative C−C and N−N Coupling of Diarylamines and Synthesis of Spiroacridines", Angewandte Chemie International Edition, Vol. 56, Issue 2, pp. 549–553.
8. GERASKIN, Ivan M., LUEDTKE, Matthew W., NEU, Heather M., NEMYKIN, Victor N., ZHDANKIN, Viktor V. (2008), ”Organic iodine(V) compounds as terminal oxidants in iron(III) phthalocyanine catalyzed oxidation of alcohols", Tetrahedron Letters, Vol. 49, Issue 52, pp. 7410–7412.
9. GROOTBOOM, Natasha, NYOKONG, Tebello (2002), "Iron perchlorophthalocyanine and tetrasulfophthalocyanine catalyzed oxidation of cyclohexane using hydrogen peroxide, chloroperoxybenzoic acid and tert-butylhydroperoxide as oxidants", Journal of Molecular Catalysis A: Chemical, Vol. 179, Issue 1–2, pp. 113–123.
10. GU, Jing-Ying, CAI, Zhen-Feng, WANG, Dong, & WAN, Li-Jun, (2016). "Single-Molecule Imaging of Iron-Phthalocyanine-Catalyzed Oxygen Reduction Reaction by in situ Scanning Tunneling Microscopy", ACS Nano, Vol. 10, Issue 9, pp. 8746–8750.
11. HASHIMOTO, Takuma, HIROSE, Daisuke, & TANIGUCHI, Tsuyoshi, (2014), "Direct Synthesis of 1,4-Diols from Alkenes by Iron-Catalyzed Aerobic Hydration and C-H Hydroxylation", Angewandte Chemie International Edition, Vol. 53, Issue 10, pp. 2730–2734.
12. HASHIMOTO, Takuma, HIROSE, Daisuke, TANIGUCHI, Tsuyoshi, (2015), "Catalytic Aerobic Oxidation of Arylhydrazides with Iron Phthalocyanine", Advanced Synthesis & Catalysis, Vol. 357, Issue 14–15, pp. 3346–3352.
13. HU, Xiaoming, XIA, Dingguo, ZHANG, Lei, & ZHANG, Jiujin (2013), "High crystallinity binuclear iron phthalocyanine catalyst with enhanced performance for oxygen reduction reaction", Journal of Power Sources, Vol. 231, pp. 91–96.
14. JIANG, Yuanyuan, Lu, Yizhong, Lv, Xiangyu, Han, Dongxue, Zhang, Qixian, Niu, Li, & Chen, Wei, (2013). "Enhanced Catalytic Performance of Pt-Free Iron Phthalocyanine by Graphene Support for Efficient Oxygen Reduction Reaction", ACS Catalysis, Vol. 3, Issue 6, pp. 1263–1271. https://doi.org/10.1021/cs4001927
15. KUDRIK, Evgeny. V., SAFONOVA, Olga, GLATZEL, Pieter, SWARBRICK, Janine C., ALVAREZ, Leonardo X., SOROKIN, Alexander B., & Afanasiev, Pavel. (2012), "Study of N-bridged diiron phthalocyanine relevant to methane oxidation: Insight into oxidation and spin states from high resolution 1s core hole X-ray spectroscopy", Applied Catalysis B: Environmental, Vol. 113–114, Issue 43–51, pp. 43-51.

16. LEGNANI, Luca, & MORANDI, Bill, (2016), “Direct Catalytic Synthesis of Unprotected 2-Amino-1-Phenylethanols from Alkenes by Using Iron(II) Phthalocyanine”, Angewandte Chemie International Edition, Vol. 55, Issue 6, pp. 2248–2251.
17. LI, Wenmu, YU, Aiping, HIGGINS, Drew C., LLANOS, Bernard G., & CHEN, Zhongwei (2010), “Biologically Inspired Highly Durable Iron Phthalocyanine Catalysts for Oxygen Reduction Reaction in Polymer Electrolyte Membrane Fuel Cells”, Journal of the American Chemical Society, Vol. 132, Issue 48, pp. 17056–17058.
18. MAHYARI, Mojtaba, & SHAABANI, Ahmad. (2014), ”Graphene oxide-iron phthalocyanine catalyzed aerobic oxidation of alcohols”, Applied Catalysis A: General, Vol. 469, pp. 524–531.
19. OBERST, Justin L., THORUM, Matthew S., & GEWIRTH, Andrew A. (2012). Effect of pH and Azide on the Oxygen Reduction Reaction with a Pyrolyzed Fe Phthalocyanine Catalyst. The Journal of Physical Chemistry C, 116(48), 25257–25261.
20. OSMIERI, Luigi, ESCUDERO-CID, Ricardo, MONTEVERDE VIDELA, Alessandro H. A., OCÓN, Pilar, & SPECCHIA, Stefania, (2018), “Application of a non-noble Fe-N-C catalyst for oxygen reduction reaction in an alkaline direct ethanol fuel cell”, Renewable Energy, Volume 115, pp. 226–237.
21. SAKA, Ece Tugba, & BIYIKLIOĞLU, Zekeriya. (2013), “Co(II) and Fe(II) phthalocyanines: Synthesis, characterization and catalytic activity on cyclohexene oxidation with different oxygen source”, Journal of Organometallic Chemistry, Vol. 745–746, pp. 50–56.
22. SHARMA, Vishal B., JAIN, Suman L., SAIN, Bir, (2004), “An Efficient Method for the Olefination of Aldehydes with Ethyl Diazoacetate Using Iron (II) Phthalocyanine as Catalyst”. Catalysis Letters, Vol. 98, Issue 2–3, pp. 141–143.
23. SINGHAL, Sweety., JAIN, Suman L., SAIN, Bir. (2010), “Heterogeneously Catalyzed Oxidative Cyanation of Tertiary Amines with Sodium Cyanide/Hydrogen Peroxide using Polymer-Supported Iron(II) Phthalocyanines as Catalyst”, Advanced Synthesis & Catalysis, Vol. 352, Issue 8, pp. 1338–1344.
24. YIN, Zhiping, WANG, Zechao, & WU, Xiao-Feng, (2017), “Iron-Catalyzed Regioselective Synthesis of 3-Arylindoles”. ChemistrySelect, Vol 2, Issue 23, pp. 6689–6692.
25. YUAN, Guang-En, LI, Yunbei, LV, Jinghua, ZHANG, Guoquan, & YANG, Fenglin, (2017), “Integration of microbial fuel cell and catalytic oxidation reactor with iron phthalocyanine catalyst for Congo red degradation”, Biochemical Engineering Journal, Volume 120, pp. 118–124.
26. ZALOMAEVA, Olga V., IVANCHIKOVA, Irina D., KHOLDEEVA, Oxana A., & SOROKIN, Alexander B. (2009). “Kinetics and mechanism of the oxidation of alkyl substituted phenols and naphthols with tBuOOH in the presence of supported iron phthalocyanine”. New Journal of Chemistry, Vol. 33, Issue 5, pp. 1031-1037.
27. ZALOMAEVA, Olga V., KHOLDEEVA, Oxana A., SOROKIN, Alexander B. (2007), “Preparation of 2-methyl-1,4-naphthoquinone (vitamin K3) by catalytic oxidation of 2-methyl-1-naphthol in the presence of iron phthalocyanine supported catalyst”, Comptes Rendus Chimie, Vol. 10, Issue 7, pp. 598–603.
28. ZHAO, Feng, HARNISCH, Falk, SCHRÖDER, Uwe, SCHOLZ, Fritz, BOGDANOFF, Peter, & HERRMANN, Iris (2006), “Challenges and Constraints of Using Oxygen Cathodes in Microbial Fuel Cells”, Environmental Science & Technology, Vol. 40, Issue 17, pp. 5193–5199.
29. ZHAO, Jun-Long, GUO, Shi-Huan, QIU, Jun, GOU, Xiao-Feng, HUA, Cheng-Wen, & Chen, Bang (2016), “Iron(III) phthalocyanine-chloride-catalyzed synthesis of sulfones from sulfonylhydrazones”. Tetrahedron Letters, Vol. 57, Issue 22, pp. 2375–2378.

CHAPTER 2

INVESTIGATION OF GAMMA AND NEUTRON RADIATION SHIELDING PROPERTIES OF VARIOUS (600-601-625-718) INCONEL ALLOYS

Bünyamin AYGÜN[1]

INTRODUCTION

With the development of industry and technology use of radiation is increasing in various areas such as nuclear power plant, agriculture, archaeology, geology, medicine, space exploration, and many others etc. Ionizing radiation is used in these applications which may cause a radiation leakthat harmful to living tissues. To prevent the radiation's damaging effects good shielding is needed. Especially in nuclear power plant the high performance shielding material is necessary because both radiation level and temperature very high in there [1]. Therefore, alloys and stainless steels are necessarily used for both excellent shielding ability and high resistance against temperature, corrosion and oxidation in the nuclear reactors. Nickel based alloys have always been an important material for many industries with high pressures, temperatures and corrosion resistance that it is a desired material. Nickel alloys have excellent corrosion and oxidation resistance in chemical applications and nuclear reactor of each temperature, (both low and high) a material that is can be weldability even in a hardened condition [2,3]. Nickel based alloys can be produced by mixing in certain proportions Fe, Cr, V, Mo etc. Materials. According to the contain materials and rates they are Inconel alloys 600,601,625 and 628 etc. Named as. Nickel based alloys such as Inconel 600, 601, 625 and 628 for their high resistance to corrosion and temperature and are used for heat tubing in the steam generators, high-temperature applications in nuclear power plants [4, 5]. To improve the safety of nuclear reactors it is necessary to study and determine the absorption and interaction of gamma and fast neutron radiation in shield materials. In order to use the Inconel alloys in radiation shielding, radiation shielding parameters must be determined. Total macroscopic section (cm^{-1}) is an important parameter in the studies of shielding neutron radiation. The mass attenuation coefficient (μ/ρ-cm^2/g), effective atomic number (Z_{eef}) and electron density are an important basic shielding parameter used to describe gamma shielding materials design [6]. The effective atomic number, which is a very important parameter for many shielding studies and this parameter can be used the properties to determine of a shield material in terms of equivalent elements. It was calculated effective atomic numbers in the different energy region of absorption for W/Cu some alloys and gamma ray shielding parameter was determined [7]. Some of the alloys, the total interaction cross-sections and effective atomic numbers were determined for especially on (Cu/Zn) alloys which have a mass combination (81.621% / 18.379%) ratio [8]. Some lead-free tungsten compounds and alloys shielding properties have been

---

[1]

determined such as the effective atomic numbers, ZPleff and half value layer, HVL for gamma ray. As well as the total macroscopic cross-sections (ΣR) for fast neutron 2 to 12 MeV energy range had been calculated. Tungsten has been found to be better at shielding against gamma rays and neutrons compared to lead [9]. In this paper, the shielding, radiation ability of Ni-based alloys (Inconel 600, 601, 625 and 718) have been evaluated. Fast neutron total macroscopic cross section values were calculated by Monte Carlo simulation Geant4 code technique and experimental absorbed dose rates were measured. Gamma ray mass attenuation coefficient and half value layer (HLV) and mean free path values were determined by WinXcom software.

Theory

The possibility of interaction of the neutrons with a single core of the target material is expressed as a microscopic cross section (σ) and barns or cm^2 units. The total macroscopic cross-section gives the possibility of interacting with all the nuclei in the volume of the target material and it is expressed as cm^{-1}. [10].

$$N = \frac{r}{A} N_A \tag{1}$$

Where the N atomic density of the target material, ρ is the density of the target material, Na is the Avogadro number, A is the interaction area of target material.

$$\sum = \sigma N \ (1/cm) \tag{2}$$

$$\sigma_t = \sigma\_scattering + \sigma\_capture + \sigma\_fission \tag{3}$$

$$\Sigma \text{ Total} = \Sigma \text{ scattering} + \Sigma \text{ absorption} + \Sigma \text{ capture} + \Sigma \text{ fission} \tag{4}$$

When a mono-energetic gamma ray interacts with the substance, there will be a decrease in energy according to the Lambert Beer law.

$$I = I_0 e^{-\left(\frac{m}{r}\right)t} \tag{5}$$

I_0, radiation intensity from source, I, radiation intensity passing through target material, (cm^{-1}) and ($cm^2 g^{-1}$) are the linear and mass attenuation coefficients (MACs), r ($g.cm^{-3}$) is the density and t (cm) is the thickness of the material.

The mean free path (MFP) which of a material of determining the radiation shielding ability and it is expressed as the average distance between two successive interactions of radiation, the mean free path is given by:

$$MFP = \frac{1}{m} \tag{6}$$

μ is the mass attenuation coefficients of materials.

The HVL is expressed as the thickness of the shielding material that halves the incoming radiation energy and can be calculated as follows:

$$HVL = \frac{\ln(2)}{m} = \frac{0.639}{m} \qquad (7)$$

MATERIAL AND METHODS

Monte Carlo Simulation Code (GEANT4)

Monte Carlo simulation Geant4 code is a very useful a kit, especially in modern particle physics for experimental and detector geometry designing and analyzing the data. It is successfully used many of radiation applications such as nuclear physics, accelerator science, astrophysics, space engineering, calculation of radiation damage, medical physics and industrial applications. The Geant4 toolkit provides a comprehensive information on nuclear physic applications in modelling the results particles interactions of materials. Geant4 gives information about the potential damages that may arise during nuclear applications and it is simulated eV to TeV energy ranges the event of electromagnetic, hadronic particles in the energy range under conditions [11].

Sample Preparation

The used powder form pure elements (Ni, Cr, Fe, C, Mn, Si, S, Cu, Ni: 99.9 weight%; Cr, Fe: 99.99 weight%) were obtained commercially. Inconel alloys were received exactly the essential elements, but the combined ratios were determined using the Monte Carlo simulation program Geant4 code. The ratios of Ni and Cr were kept to a maximum weight in the determination of the ratio of the alloying elements in the mass, because these two elements have a high cross-section of neutron radiation. Powder metallurgy method was used in the production and all Inconel alloy samples were made pelletized by hydraulic press machine at 600 MPa pressure, which have 10 g weight, 2 cm diameter. The all alloy samples were annealed at 1250 ^{0}C for 8 hours, then hardened by the rapid cooling process. The contents and mass percentages of the produced Inconel alloy samples are shown in Table 1.

Table 1. Chemical compositions of the Inconel alloys (%) Sample

Element	600 ρ=8.47 (g/cm^3)	601 ρ=8.11 (g/cm^3)	625 ρ=8.44 (g/cm^3)	718 ρ=8.19 (g/cm^3)	316LN ρ=8.1 (g/cm^3)
Ni	70.35	63	63.92	55	14
Cr	17	25	23	21	18
Fe	10	8.88	5	13.42	61.985
C	0.15	0.10	0.10	0.08	0.030
S	0.015	0.015	0.015	-	0.030
Mn	1	0.5	0.5	0.35	2
Si	0.5	0.5	0.5	0.35	0.75
Cu	0.5	1	-	-	-
Al	-	1	0.4	0.8	-
Mo	-	-	1	2.8	3
Nb+Ta	-	-	4.15	4.75	-
B	-	-	-	0.006	-
P	-	-	0.015	0.015	0.045
Co	-	-	1	0.3	-
Ti	-	-	0.4	1.15	-
N	-	-	-	-	0.16

Experimental Design

Fast neutron absorbed dose measurements of the samples were calculated using a ^{241}Am-Be neutron source with an average of 4.5 MeV effective neutron energy and CANBERRA portative type BF_3 gaseous detector. As shown in Figure 1. Absorption dose measurement system was designed. Samples were placed between detector and source, each sample was bombarded for 20 minutes. Dose rates absorbed by the sample were determined.

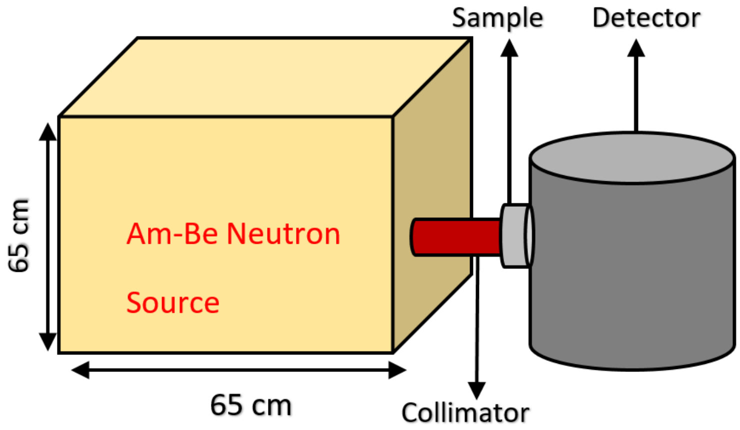

Figure 1 Neutron absorption dose measurement system

RESULT AND DISCUSSION

NEUTRON SHIELDING PARAMETERS

Total Macroscopic Cross Section

Shielding parameters such as the macroscopic cross section (cm^{-1}), Mean free path and transmission values were calculated of Inconel alloys (600,601,625,718) for fast neutron by Monte Carlo simulation Geant4 code. When neutrons interact with material elastic scattering or inelastic scattering might occur or neutrons might be captured by the core of the material. The possibility of making these interactions with the substance of neutrons is expressed by the macroscopic cross section (cm^{-1}). Neutrons can be stopped by these interactions with the substance, of a material macroscopic cross section gives information about the characteristics of the shielding. The greater the value of the material, the greater the neutron stopping force of the material [12-13].

Mean Free Path

The mean free path is defined as the mean path travelled by a neutron between two collisions determined by the symbol λ. Both the high macroscopic cross-section and the very short mean free paths materials have excellent neutron absorption capabilities and this shielding are usually occur on the surface of the material [14-15].

Transmission

All samples were bombardment with 100000 neutrons and passing neutron numbers were determined from samples. Neutron low transmission number is showing shielding ability and this it means neutron stopping power of target sample is higher.

As shown in Table 2 and Fig.2. The results were compared with 316LN stainless steel which, it is used in nuclear applications commonly. Simulation results show that the four Inconel alloy (600A, 601B, 625C, 718D) sample has high Total macroscopic cross section values and lower mean free paths which is better than 316LN stainless steel.

Table 2 Total macroscopic cross sections, Mean Free Path, Transportation values of samples

Sample code	Total macroscopic cross section (cm^{-1})	Mean Free Path	Transmission
316LN	0.3014	4.7642+-2.8831	73511
600A	0.3207	4.7406+-2.8735	72559
601B	0.3157	4.7421+-2.8847	72925
625C	0.3189	4.7558+-2.8929	72689
718D	0.3100	4.7404+-2.8765	73344

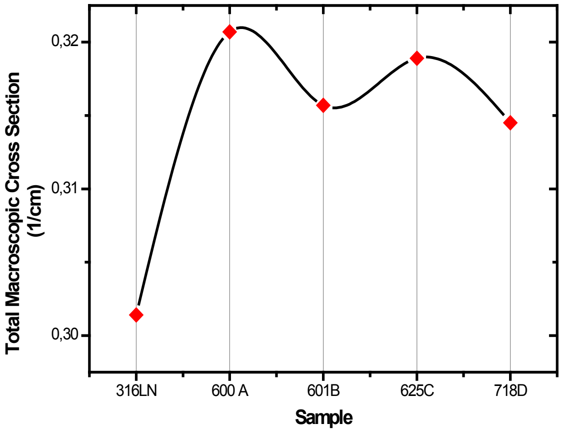

Figure 2. Theory 4.5 MeV Neutron Total Macroscopic Cross Section (cm^{-1})

Absorption Dose Measurements

Neutron absorption dose measurements were carried out. Absorbed dose values were calculated and he obtained results were compared with paraffin and 316LN stainless steel which usually used shielding radiation applications as shown in Table 3.

Table 3 Absorbed Dose Rates by Experiments

Sample code	Absorbed equivalent dose rates (µSv/h) by the samples	Absorbed dose percentage of samples (%)
Paraffin	0.5738	40.89
316LN	0.4074	29.03
600	0.5103	36.36
601	0.4758	33.90
625	0.5039	35.91
718	0.4502	32.08

As shown in Table 3 it was observed that the dose of 1.4032 (µSv/h) emitted from the source was absorbed paraffin (40.89%), 316LN (29.03%), Inconel 600 (36.36%), Inconel 601 (33.90%), Inconel 625 (35.91%) and Inconel 718 (32.08%) of the dose. According to the results, all Inconel alloy samples show good shielding ability, Thus Inconel alloys (600,601,625,718) having excellent corrosion, high temperature and oxidation resistance can be used instead of 316LN stainless steel in nuclear applications.

GAMMA RADIATION SHIELDING PARAMETERS

The Theoretical Mass Attenuation Coefficients (MACs) and Half Value Layer (HVL) and Mean free path (cm)

In this study, it has been calculated the gamma radiation shielding parameters of the Inconel alloys (600,601,625,718) in the energy range between 0.015 and 10 MeV by using WinXcom software. As shown in Fig. 3.4.5 and in Table 4.5.6. The obtained result of mass attenuation coefficients (MACs), Half Value Layer (HVL) and Mean free path (cm) results were compared with 316LN stainless steel.

Table 3 Mass attenuation coefficient (cm^2/g) values of samples

Energy (MeV)	**Mass attenuation coefficient (cm^2/g)**				
	600	**601**	**625**	**718**	**316LN**
0,015	64,567	62,239	18,803	61,284	55,479
0,02	29,261	28,173	10,581	31,434	26,972
0,03	9,372	9,015	3,534	10,216	8,673
0,04	4,167	4,008	1,653	4,575	3,865

0,05	2,245	2,161	0,948	2,474	2,088
0,06	1,375	1,326	0,623	1,517	1,284
0,08	0,671	0,649	0,471	0,853	0,631
0,1	0,412	0,401	0,317	0,513	0,391
0,15	0,210	0,207	0,186	0,244	0,203
0,2	0,153	0,151	0,144	0,168	0,149
0,3	0,113	0,112	0,112	0,118	0,111
0,4	0,096	0,096	0,097	0,098	0,094
0,5	0,086	0,086	0,087	0,087	0,084
0,6	0,079	0,078	0,080	0,079	0,077
0,8	0,068	0,068	0,069	0,068	0,067
1	0,061	0,061	0,062	0,061	0,060
1,5	0,050	0,050	0,051	0,049	0,049
2	0,043	0,043	0,044	0,043	0,043
3	0,037	0,037	0,036	0,037	0,036
4	0,034	0,034	0,032	0,034	0,033
5	0,032	0,032	0,029	0,032	0,032
6	0,031	0,031	0,027	0,032	0,031
8	0,031	0,031	0,025	0,031	0,030
10	0,031	0,031	0,024	0,031	0,030

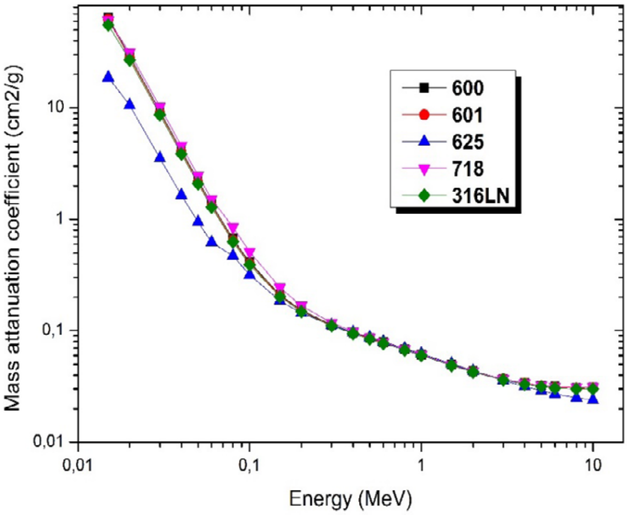

Figure 3. The mass Attenuation Coefficients of the Samples

It is clearly seen that the MACs of the Inconel alloys are higher than the 316LN stainless steel in all calculated energies.

Table 4. Half value layer (cm) of the Samples

Half value layer (cm)					
Energy (MeV)	**600**	**601**	**625**	**718**	**316LN**
0,015	0,001	0,001	0,004	0,001	0,002
0,02	0,003	0,003	0,008	0,003	0,003
0,03	0,009	0,009	0,023	0,008	0,010
0,04	0,020	0,021	0,050	0,018	0,022
0,05	0,036	0,040	0,087	0,034	0,041
0,06	0,060	0,064	0,132	0,056	0,067
0,08	0,122	0,132	0,174	0,099	0,137
0,1	0,198	0,213	0,259	0,165	0,222
0,15	0,389	0,414	0,442	0,347	0,428
0,2	0,534	0,565	0,569	0,504	0,582
0,3	0,723	0,760	0,733	0,719	0,782
0,4	0,850	0,892	0,849	0,863	0,917

0,5	0,952	0,998	0,945	0,977	1,026
0,6	1,042	1,092	1,030	1,074	1,122
0,8	1,200	1,256	1,182	1,243	1,291
1	1,341	1,405	1,320	1,393	1,444
1,5	1,647	1,725	1,623	1,714	1,773
2	1,884	1,974	1,879	1,960	2,029
3	2,213	2,321	2,288	2,296	2,389
4	2,414	2,534	2,600	2,498	2,611
5	2,534	2,663	2,840	2,616	2,747
6	2,602	2,738	3,026	2,682	2,826
8	2,650	2,792	3,283	2,722	2,886
10	2,639	2,785	3,438	2,705	2,881

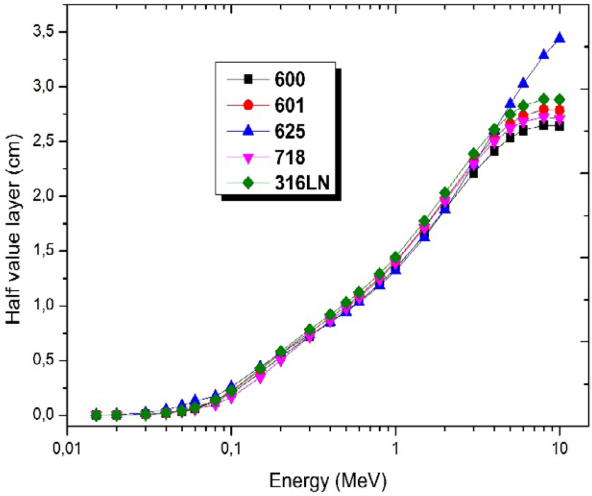

Figure 4. Variation of HVL with photon energy in the energy region 0.015 and 10 MeV

The values of the HVL of the samples are presented in the Fig. 4. and Table 4. With increasing energy, HVL values of Inconel alloys are increasing and this is a result that compatible with 316LN.

Table 5. Mean free path (cm) of the Samples

Mean free path (cm)					
Energy (MeV)	**600**	**601**	**625**	**718**	**316LN**
0,015	0,002	0,002	0,006	0,002	0,002
0,02	0,004	0,004	0,011	0,004	0,005
0,03	0,013	0,014	0,034	0,012	0,014
0,04	0,028	0,031	0,072	0,027	0,032
0,05	0,053	0,057	0,125	0,049	0,060
0,06	0,086	0,093	0,190	0,080	0,097
0,08	0,176	0,190	0,251	0,143	0,198
0,1	0,286	0,308	0,374	0,238	0,320
0,15	0,561	0,597	0,637	0,501	0,617
0,2	0,771	0,815	0,820	0,727	0,840
0,3	1,043	1,096	1,058	1,037	1,128
0,4	1,227	1,287	1,225	1,246	1,323
0,5	1,374	1,440	1,363	1,409	1,481
0,6	1,503	1,575	1,486	1,549	1,619
0,8	1,731	1,813	1,705	1,793	1,863
1	1,935	2,027	1,904	2,010	2,083
1,5	2,376	2,488	2,342	2,472	2,557
2	2,719	2,848	2,710	2,827	2,928
3	3,193	3,348	3,301	3,312	3,446
4	3,482	3,656	3,751	3,604	3,766
5	3,656	3,842	4,098	3,775	3,963
6	3,754	3,949	4,366	3,869	4,077
8	3,822	4,028	4,736	3,927	4,164
10	3,808	4,017	4,960	3,903	4,157

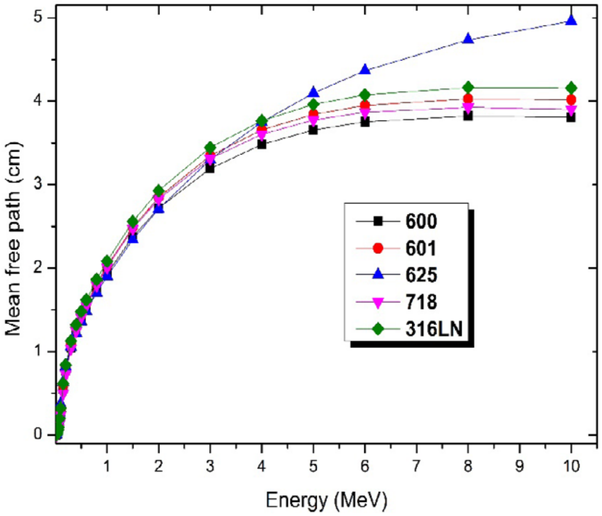

Figure 5. Mean free path (cm) of the Samples

The average free path is the distance a gamma ray travels in the target material before it is absorbed. This measured value is small indicates that the material has high power to absorb the gamma rays. According to the results of Inconel alloy (600, 601, 718) gamma shielding ability better than 316 LN stainless steel was determined.

CONCLUSION

In the present work, to improve the safety of nuclear reactors it is necessary to study and determine the absorption and interaction of gamma and fast neutron radiation in shield materials. We were produced, four different type Inconel alloy (600,601,625,718) samples with high nickel content and equivalent absorbed dose measurement was carried out, absorbed dose rates were determined using 4.5 MeV energy Am-Be neutron source. In addition, Monte Carlo Simulation Geant4 code and WinXCOM software we have calculated the total macroscopic cross section (TMCS), of the Inconel alloys samples theoretically. The results were compared with paraffin and 316LN stainless steel. It is found that neutron total macroscopic cross section (TMCS), gamma mass attenuation coefficients (MACs) values of Inconel alloy were higher than on 316LN stainless steel but lower than paraffin. The calculated mass attenuation coefficients (MAC), half value layer (HVL) and Mean free path (cm) results compared with 316 LN stainless steel. According to these results, it was determined that four different content Inconel alloy samples could be used instead of 316LN stainless steel for radiation safety in research laboratory, nuclear reactor, shelters and radiation therapy centers.

Acknowledgements

This work is financially supported by University of Atatürk with Grant No. 2016/FM7, FBA-2017-6312 and University of Agri Ibrahim Cecen with Grant no. MYO.18.001.

REFERENCES

1. Technical and Economic Aspects of Load Following with Nuclear Power Plants, OECD Nuclear Energy Agency (June 2011)
2. A.Thakur, S. Gangopadhyay. State-of-the-art in surface integrity in machining of nickel-based super alloys. International Journal of Machine Tools and Manufacture. Volume 100, January 2016, Pages 25-54
3. Gopala Rao Thellaputta, Pulcharu Subhash Chandra, C.S.P. Rao. Machinability of Nickel Based Super alloys: A Review. Materials Today: Proceedings. Volume 4, Issue 2, Part A, 2017, Pages 3712-3721
4. COPSON H. R., BERRY W. E. 2013. Qualification of Inconel For Nuclear Power Plant Applications. CORROSION. 1960;16 (2):79t-85t.
5. Manoj Kumar.2012. Materials for High Temperature Nuclear Applications National Seminar on "INDIAN Nuclear Programme, Challenges and Opportunities –INCO -12
6. R. El-Mallawany, M.I. Sayyed, M.G. Dong. 2017. Comparative shielding properties of some tellurite glasses: Part 2, Journal of Non-Crystalline Solids 474, 16–23
7. Murty VRK. Effective atomic numbers for W/Cu alloy for total photon attenuation. Rad Phys and Chem 2004;71:667–9.
8. El-Kateb AH, Rizk RAM, Abdul-Kader AM. Determination of atomic cross-sections and effective atomic numbers for some alloys. Annals of Nuclear Energy 2000;27:1333–43.
9. V. P. Singh, N. M. Badiger. An Investigation on Gamma and Neutron Shielding Parameters for Lead Free Compounds and Alloys. Indian Journal of Pure & Applied Physics. 54, 2016, 443-448
10. Raghep, M. Neutron Cross Section. 2017. mragheb.com
11. Agostinelli, S., et al., 2003. Geant4—a simulation toolkit. Nucl. Instr. Methods Phys. Res A. 506 (3), 250-303.
12. K. O. Ott, W. A. Bezella, Introductory Nuclear Reactor Statics, American Nuclear Society, Revised edition (1989), 1989, ISBN: 0-894-48033-2.
13. K. O. Ott, R. J. Neuhold, Introductory Nuclear Reactor Dynamics, American Nuclear Society, 1985, ISBN: 0-894-48029-4.
14. J. R. Lamarsh, Introduction to Nuclear Reactor Theory, 2nd ed., Addison-Wesley, Reading, MA (1983).
15. J. R. Lamarsh, A. J. Baratta, Introduction to Nuclear Engineering, 3d ed., Prentice-Hall, 2001, ISBN: 0-201-82498-1.

CHAPTER
3

ANALYSES OF INTERFACE STATES AND SERIES RESISTANCE EFFECT ON THE AU/4H-SIC SBDS

Dilber Esra Yıldız

Experimental Methods

Under this work, Au/4H n-SiC SBDs were fabricated on the n-type SiC substrates. They are about 500 μm thick, in single-crystalline phase with (0001) orientation and doped with nitrogen concentration of around 3.2×10^{16} cm^{-3}. Before the formation of Au contacts, the wafer substrates were ultrasonically cleaned under the chemical treatments with $CHClCCl_2$, CH_3COCH_3, and CH_3OH for 10 minutes. Then, wet etching procedure was applied to the surface of the wafers in a sequence of H_2SO_4 and H_2O_2 20% HF, 20% HF, a solution of $6HNO_3{:}1HF{:}35H_2O$, and as a final step they were rinsed in de-ionized water with 18 MΩ.cm resistivity. The ohmic back contacts were developed on the 4H n-SiC substrates in order to carry on the electrical measurements. 200 nm thick metal contacts were deposited by thermal evaporation of Au (99.999% pure) at the substrate temperature of 450 ^{o}C in high vacuum condition (10^{-7} mbar). After this process, post-heat treatment was applied to the samples at 400 ^{o}C in order to enhance the ohmic contact behavior on the surface of the substrates. As a rectifying contact, 150 nm thick Au metal contact were also thermally evaporated on the front surface of the substrates through the 2 mm diameter dot shaped shadow masks. The schematic illustration and energy band diagram of the fabricated Au/4H n-SiC SBDs were given in Fig. 1. The electrical characterization of these SBDs were investigated under the C-V and G/w-V measurements by using Keithley 4200 SCS semiconductor characterization system.

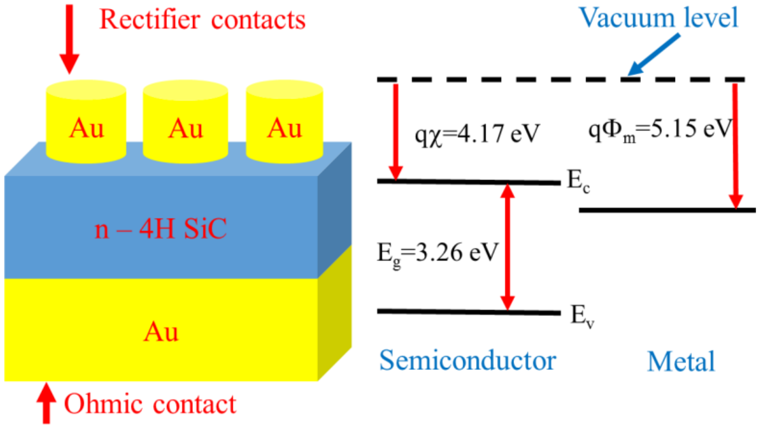

Fig. 1. The schematic and energy level diagrams of Au/4H n-SiC SBDs.

Results and Discussion

The room temperature C-V and G/w-V plots of Au /4H n-SiC SBDs at frequency range of 1 kHz to 1000 kHz were shown in Fig.2 and Fig.3, respectively. As seen Fig.2, *C* values has an anomalous peak in the region of interest, and the magnitude of these peaks were observed in increasing behavior with decrease in frequency. The origin of these peaks in the C-V plots can

be related with the presence of N_{ss} [20] and also R_s can affect this behavior of the Au /4H n-SiC SBDs in the forward bias region. [21]. However, variation in R_s can only be attributed to the downward curvature of the C-V plots. The measured *G/w* values with respect to the applied voltage at different frequencies were shown in Fig.3. In this figure, when the frequency increases from 1 kHz to 1000 kHz, the G/w-V plots for high frequencies and reverse bias voltages reach stationary values. As a result of these analyses, N_{ss} and R_s can be responsible for the observed frequency dispersion in G/w-V plots of Au/4H n-SiC SBDs under bias voltage [21-23].

In order to determine the R_s values, Nicollian and Goetzberger technique was applied to the experimental results [12,19,24]. According to this technique, R_s can be calculated from the measured capacitance (C_{ma}) and conductance (G_{ma}) values. The measured impedance (Z_{ma}) at strong accumulation of fabricated MS SBDs equals to the total circuit impedance as;

$$Z_{ma} = \frac{1}{G_{ma} + j\omega C_{ma}} \tag{1}$$

Comparing the real and imaginary part of the impedance, R_s is given by [21]

$$R_s = \frac{G_{ma}}{G_{ma}^2 + (\omega C_{ma})^2} \tag{2}$$

where C_{ma} and G_{ma} are the measured capacitance and conductance in strong accumulation region, respectively. The capacitance of insulator oxide layer, C_{ox} is related with R_s and thickness of insulator layer and then, it can be expressed as;

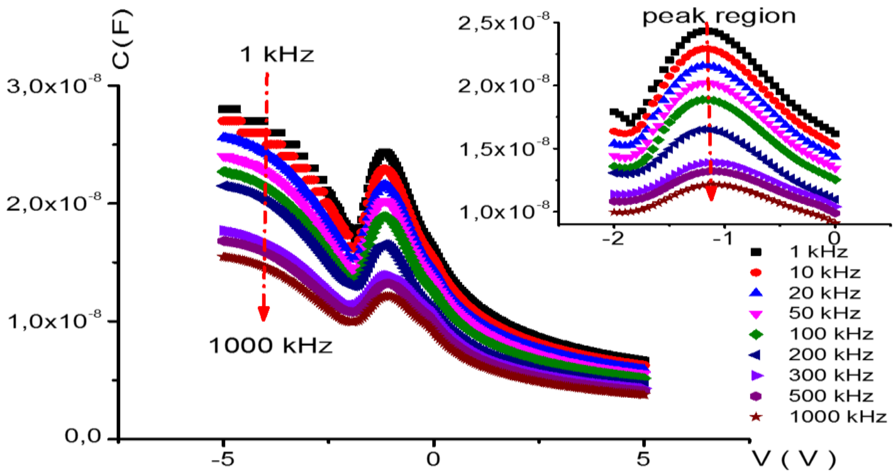

Fig. 2. The capacitance C (V,f) of Au/4H n-SiC SBDs at verious frequency.

$$C_{ox} = C_{ma}\left[1+\left(\frac{G_{ma}}{\omega C_{ma}}\right)^2\right] = \frac{\varepsilon_i \varepsilon_o A}{d_{ox}} \tag{3}$$

where ε_i and ε_o are the permittivity of the interfacial insulator layer and free space, respectively.

The calculated R_s values of Au /n-type 4H-SiC SBDs by using Eq. (2) were plotted in Fig. 4 under the effect of change in the applied frequency. As given in Fig. 4, these values are observed in inversely proportional to applied voltage and also to frequency. These decreasing characteristics of R_s were found rapidly in the range of (-2 V) – (0 V). As observed from Fig. 4, R_s is nearly independent of the bias voltage at high frequencies. The carriers have adequate energy to escape from the traps located between metal and semiconductor interface in the 4H-SiC band gap and as a result, R_s depends on the changes in both frequency and voltage from region to region. Otherwise, the charges at the interface states cannot follow the ac signal at high frequencies [22,23].

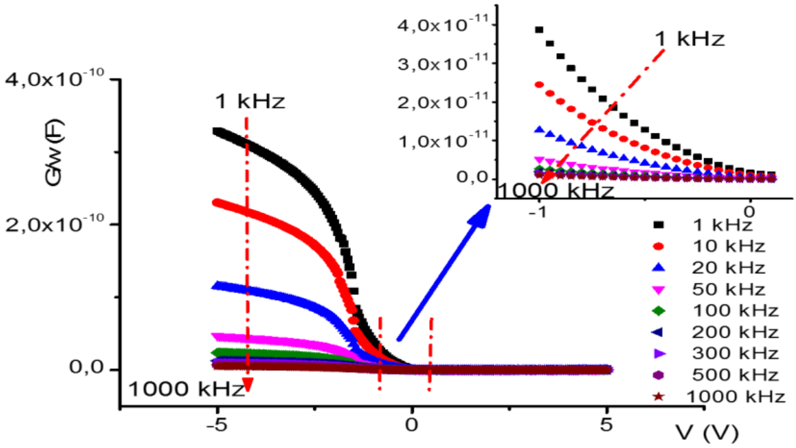

Fig. 3. Equivalent parallel conductance G(V,f) of Au/4H n-SiC SBDs at various frequency.

Furthermore, Hill-Coleman single frequency conductance *technique* was used for the determination of N_{ss} values. In this technique, the N_{ss} values are expressed as [25]:

$$N_{ss} = \left(\frac{2}{qA}\right)\frac{(G_m/\omega)_{\max}}{(G_m/\omega)_{\max}C_{ox})^2 + (1 - C_m/C_{ox})^2} \tag{4}$$

where w is the angular frequency, A is the area of diode, C and $(G/w)_{max}$ are the measured C and G/w corresponding to the peak values, respectively. In this analysis, C_{ox} can be obtained from C-V and G/w-V measurements at high frequency region. Therefore, from these analyses,

N_{ss} values determined from these measurements in the frequency range of 1 kHz-1000 kHz were tabulated in Table 1. In addition, the frequency dependence of N_{ss} was plotted in Fig. 5. The frequency dependence of the N_{ss} values can be clearly seen from Fig. 5. This dependence

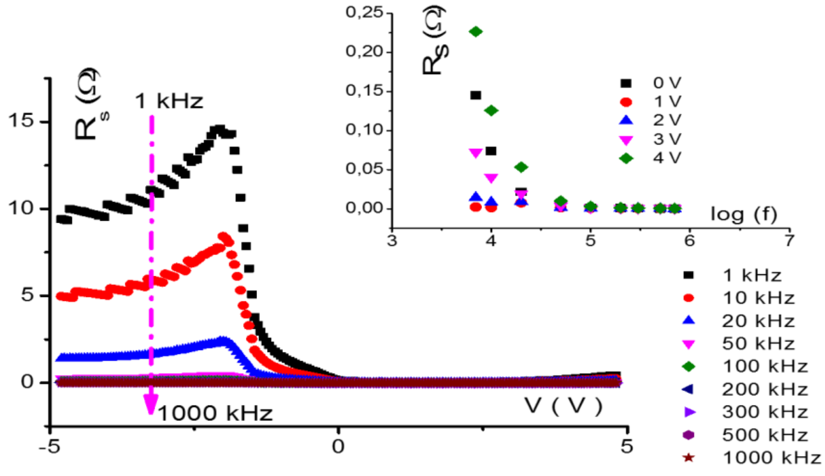

Fig. 4. R_s vs. V and R_s vs. log (f) plots of Au /4H n-SiC SBDs.

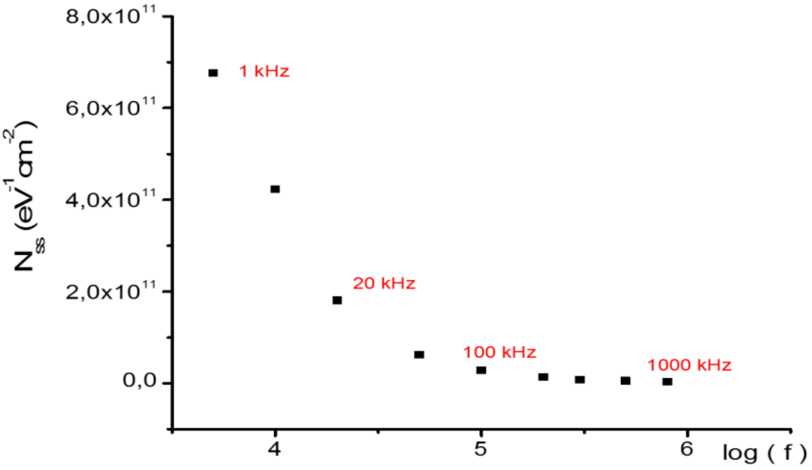

Fig. 5. Variation of N_{ss} as a function of frequency of Au /4H n-SiC SBDs.

can trigger the increase in the C of the diode at low frequencies, however the effect of frequency variation at high frequencies cannot dominate the N_{ss} characteristics. The high values of C can be referred to the excess capacitance resulting from N_{ss}, which is in equilibrium with the semiconductor and follows the ac signal at low frequencies [22,23,26].

In addition to these calculations, several electrical parameters of Au/4H n-SiC SBDs can be obtained by utilizing the linear region of C^{-2}-V plots. The C^{-2} values are linear in applied bias region for the following equation as [23];

$$C^{-2} = \frac{2(V_R + V_i)}{q\varepsilon_s N_d A^2} \tag{5a}$$

The slope of reverse- bias C^{-2}-V plot can also be given by

$$\frac{d(C^{-2})}{dV} = \frac{2}{q\varepsilon_s N_d A^2} \tag{5b}$$

where N_d is the doping concentration, V_i is the built-in voltage at zero bias, V_R is the reverse bias voltage, ε_s is dielectric constant of the SiC and q is the electronic charge.

The value of the barrier height $\Phi_B(C_m\text{-}V)$ can be determined by the relation,

$$\phi_{\mathrm{Bo}}(C_m - V) = V_i + E_F - \Delta\phi_B \tag{6a}$$

where

$$V_i = V_o + \frac{kT}{q} \tag{6b}$$

and E_F is the Fermi energy and can be determined as

$$E_F = \frac{kT}{q} In(\frac{N_c}{N_d}) \tag{7}$$

where N_c is the effective density of states in SiC conduction band and it is approximated as N_c=1.23x10^{19} cm^{-3} for effective density of states in the conduction band for 4H n-SiC at 300 K [27]. In Eq. (6a), the image force barrier lowering $\Delta\phi_B$ can be expressed as [28]

$$\Delta\Phi_B = \left[\frac{qE_m}{4\pi\varepsilon_s\varepsilon_o}\right]^{1/2} \tag{8a}$$

and

$$E_m = \left[\frac{2qN_d V_o}{\varepsilon_s\varepsilon_o}\right]^{1/2} \tag{8b}$$

Based on the result of analyses to determine the values of $\Delta\Phi_B$, E_F and V_i, $\phi_{Bo}(C_m\text{-}V)$ can be calculated as,

$$\Phi_{\mathrm{Bo}}(C_m - V) = V_o + \frac{kT}{q} + \frac{kT}{q} In(\frac{N_c}{N_d}) - \Delta\Phi_B \tag{9}$$

The depletion layer width w_d for both of the samples were also calculated from the following equation [29-31],

$$W_d = \sqrt{\frac{2\varepsilon_s \varepsilon_o V_d}{qN_d}} \quad (10)$$

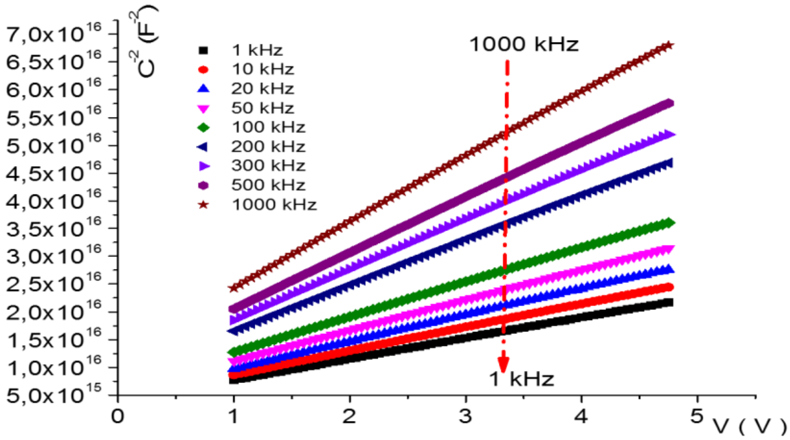

Fig. 6. Experimental $1/C_m^2$ vs. V plots of Au /4H n-SiC SBDs at various frequencies.

By using there relations, the obtained electrical parameters as N_d, V_i, E_F, w_d, $\Delta\Phi_B$ and $\Phi_{Bo}(C\text{-}V)$ were given in Table 1.

Fig. 6 shows the C^{-2}-V plots carried out in the frequency range of 1 kHz-1000 kHz. These plots indicates linear characteristics as observed from this figure. The slope of the straight line and in addition to this, $\Phi_{Bo}(C\text{-}V)$ values calculated from the C-V plots were found to be dependent on change in applied frequency (Table 1). As given in Table 1, the values $\Phi_{Bo}(C_m\text{-}V)$ at 1000 kHz is 1.150 eV which is higher than the value of 1.034 eV at 1 kHz. The variation of Φ_{Bo} may be due to modification in surface roughness of samples used, formation on interfacial layer and/or defects present the film structure, interface states at M/S interface and the presence of several transport mechanisms.

Table 1. The values of various parameters of Au/4H n-SiC SBDs determined from C_m^{-2}-V plots in the frequency range of 1 kHz-1000 kHz.

Conclusion

In this study, the frequency-dependent C-V and G/w characteristics of Au/4H n-SiC SBDs were investigated in the frequency range of 1-1000 kHz. The measured values of *C* and *G/w* in all voltage region were found in decreasing behavior with increase in frequency. The C-V plots exhibit anomalous peaks at forward bias in the range (-2 V) to (0 V) due to the presence of N_{ss} and R_s. Depending on the relaxation time of N_{ss} and the frequency of the applied ac signal, this behavior can be explained by characteristics of N_{ss} in the SBDs in which they can follow the ac signal and yield an excess capacitance. In addition, the Φ_{Bo} and w_d were calculated from C-V relation and under the effect of change in the applied frequency, these values were found in the range of 1.034-1.150 eV and $1.73x10^{-4}$-$3.09x10^{-4}$ cm, respectively. Experimental results indicate frequency dependence in the obtained Φ_{Bo} values. Furthermore, the increase in Φ_{Bo} with increasing frequency can be attributed to spatial variations of Φ_{Bo} at the interface.

f **(kHz)**	V_i **(V)**	N_d 10^{16}x(cm^{-3})	E_f **(eV)**	$\Delta\Phi_b$ **(meV)**	Φ_b (C_m-V) **(eV)**	W_d 10^{-4}x (cm)	N_{ss} (eV^{-1}cm^{-2})
1	-1.093	3.93	0.093	152.13	1.034	1.73	$6.77x10^{11}$
10	-1.093	3.48	0.096	143.18	1.046	1.84	$4.23x10^{11}$
20	-1.093	3.08	0.099	134.76	1.057	1.95	$1.81x10^{11}$
50	-1.092	2.71	0.102	126.30	1.068	2.08	$6.23x10^{10}$
100	-1.093	2.36	0.105	117.96	1.080	2.23	$2.80x10^{10}$
200	-1.092	1.82	0.112	103.46	1.101	2.54	$1.35x10^{10}$
300	-1.115	1.65	0.115	99.44	1.130	2.70	$7.33x10^{9}$
500	-1.115	1.48	0.117	94.47	1.138	2.84	$5.07x10^{9}$
1000	-1.110	1.25	0.121	86.91	1.150	3.09	$3.47x10^{9}$

References

[1] *Morkoç H.* , *Strite S.* , *Gao G. B.*, *Lin M. E.*, *Sverdlov B.* & *Burns M.* (1994) Large-band-gap SiC, III-V nitride and II-VI ZnSe-based semiconductor device technologies *J. Appl. Phys. 76*(3), *1363*–1398, https://doi.org/10.1063/1.358463

[2] Masri P. (2002) Silicon carbide and silicon carbide-based structures: The physics of epitaxy Surf. Sci. Rep. 48, 1-51, https://doi.org/10.1016/S0167-5729(02)00099-7

[3] Casady J. B.& Johnson R.W. (1996) Status of silicon carbide (SiC) as a wide-bandgap semiconductor for high-temperature applications: A review, Solid-State Electron. 39(10), 1409-1422, https://doi.org/10.1016/0038-1101(96)00045-7

[4] Liaw P. &Davis R. F. (1985) Epitaxial Growth and Characterization of β - SiC Thin Films J. Electrochem. Soc. 132(3), 642-648, https://doi.org/10.1149/1.2113921

[5] *Mehregany M.*, *Zorman C. A.*, *Rajan N.* & *Wu C. H.* (*1998*) Silicon carbide MEMS for harsh environments *Proceedings of the IEEE 86*(8), *1594*-1609, https://doi.org/10.1109/5.704265

[6] Gammon P. M., Tomas A. P., Shah V. A., Roberts G. J., Jemmings M. R., Covington J. A. & Mawby P. A. (2009) Analysis of inhomogeneous Ge/SiC heterojunction diodes J. Appl. Phys. 106, 093708, https://doi.org/10.1063/1.3255976

[7] Saxena V., Su J. N. & Steckl A. J. (1999) Visible and infrared rare-earth-activated electroluminescence from indium tin oxide Schottky diodes to GaN: Er on Si, IEEE Trans. Electron. Dev. 46(3), 456-464, https://doi.org/10.1063/1.123286

[8] Yıldız D.E., Apaydın D. H., Toppare L. & Cirpan A. (2017) Effect of layer thickness on the electrical parameters and conduction mechanisms of conjugated polymer-based heterojunction diode J. Appl. Polym. Sci. 134 (19), 44817-7, https://doi.org/10.1002/app.44817

[9] Huang C. H., Tseng T. Y., Chien C. H., Yang M. J., Leu C. C., Chang T. C., Liu P. T. & Huang T. Y. (2002) Electrical properties of metal–ferroelectric–insulator–semiconductor using sol–gel derived $SrBi_2Ta_2O_9$ film and ultra-thin Si_3N_4 buffer layer Thin Solid Films 420-421, 377-381

[10] Kumari N., Pari J., Varma K. B. R. & Krupandhi S. B. (2006) *C*–*V* studies on metal–ferroelectric bismuth vanadate ($Bi_2VO_{5.5}$)–semiconductor structure Solid State Com. 137, 566-569, https://doi.org/10.1016/j.ssc.2005.11.043

[11] Pontes F. M., Leite E. R., Lee E. J. H., Longo E. & Varela J. A. (2001) Dielectric properties and microstructure of $SrTiO_3$/$BaTiO_3$ multilayer thin films prepared by a chemical route Thin Solid Films 385(1-2), 260-265, https://doi.org/10.1016/S0040-6090(01)00772-6

[12] Nicollian E. H. & Brews J. R. (1982) Metal Oxide Semiconductor (MOS) Physics and Technology, Wiley, New York

[13] Depas M., Van Meirhaeghe R. L., Laflere W. H. & Cardon F. (1994) Electrical characteristics of Al/SiO2/n-Si tunnel diodes with an oxide layer grown by rapid thermal oxidation Solid-State Electron. 37(3), 433-441, https://doi.org/10.1016/0038-1101(94)90009-4

[14] Card H. C. & Rhoderick E. H. (1971) Studies of tunnel MOS diodes I. Interface effects in silicon Schottky diodes J. Phys. D: Appl. Phys. 4(10), 1589-1601

[15] Kelberlau U. & Kassing R. (1979) Theory of nonequilibrium properties of MIS capacitors including charge exchange of interface states with both bands Solid State Electron. 22(1), 37-45, https://doi.org/10.1016/0038-1101(79)90169-2

[16] Kuhn M. (1970) A quasi-static technique for MOS *C-V* and surface state measurements

Solid State Electron. 13(6), 873-885, https://doi.org/10.1016/0038-1101(70)90073-0

[17] Kar S. & Varma S. (1985) Determination of silicon-silicon dioxide interface state properties from admittance measurements under illumination J. Appl. Phys. 58(11), 4256-4266, https://doi.org/10.1063/1.335561

[18] K. K. Hung & Y. C. Cheng (1987) Characterization of Si-SiO_2 interface traps in p-metal-oxide-semiconductor structures with thin oxides by conductance technique J. Appl. Phys. 62(10), 4204 https://doi.org/10.1063/1.339091

[19] Nicollian E. H.& A. Goetzberger (1965) MOS Conductance Technique For Measuring Surface State Parameters Appl. Phys. Lett. 7, 216-219, https://doi.org/10.1063/1.1754385

[20] Ho P. S., Yang E. S., Evans H. L. & Wu X. (1986) Electronic states at silicide-silicon interfaces Phys. Rew. Lett. 56, 177-180, https://doi.org/10.1103/PhysRevLett.56.177

[21] Chattopadhyay P.& Raychaudhuri B. (1992) Origin of the anomalous peak in the forward capacitance-voltage plot of a Schottky barrier diode Solid-State Electron. 35, 875-878, https://doi.org/10.1016/0038-1101(92)90290-S

[22] Parlakturk F., Altındal S., Tataroglu A., Parlak M. & Agasiev A. (2008) On the profile of frequency dependent series resistance and surface states in Au/$Bi_4Ti_3O_{12}$/SiO_2/n-Si(MFIS) structures Microelectron. Eng. 85, 81-88, https://doi.org/10.1016/j.mee.2007.03.012

[23] Kanbur H., Altındal S., Tataroglu A. (2005) The effect of interface states, excess capacitance and series resistance in the Al/SiO2/p-Si Schottky diodes Appl. Surf. Sci. 252, 1732-1738, https://doi.org/10.1016/j.apsusc.2005.03.122

[24] Nicollian E. H., Goetzberger A. (1967) The si-sio, interface – electrical properties as determined by the metal-insulator-silicon conductance technique Bell Syst. Tech. J. 46, 1033-1055, https://doi.org/10.1002/j.1538-7305.1967.tb01727.x

[25] Hill W. A. & Coleman C.C. (1980) A single-frequency approximation for interface-state density determination Solid State Electron. 23, 987-993, https://doi.org/10.1016/0038-1101(80)90064-7

[26] Bülbül M. M. & Zeyrek S. (2006) Frequency dependent capacitance and conductance–voltage characteristics of Al/Si_3N_4/*p*-Si(1 0 0) MIS diodes Microelectron. Eng. 83, 2522-2526, https://doi.org/10.1016/j.mee.2006.06.002

[27] Gülen Y., Ejderha K., Nuhoğlu Ç. & Türüt A. (2011) Schottky barrier height modification in Au/n-type 6H–SiC structures by PbS interfacial layer Microelectron. Eng. 88, 179-182, https://doi.org/10.1016/j.mee.2010.10.009

[28] Kelberlau U. & Kassing R. (1979) Theory of nonequilibrium properties of MIS capacitors including charge exchange of interface states with both bands Solid State Electron. 22(1), 37-45, https://doi.org/10.1016/0038-1101(79)90169-2

[29] Yakuphanoglu F. (2007) The current–voltage characteristics of FSS/n-Si heterojunction diode under dark and illumination Physica B 388 (1–2), 226–229, https://doi.org/10.1016/j.physb.2006.05.430

[30] Yildiz D. E.& Kanbur Cavuş H. (2016) Electrical properties of Al/p-Si structure with Al_2O_3 thin film fabricated by atomic layer deposition system Surf. Rev. and Lett., 24(6), 1750077, https://doi.org/10.1142/S0218625X17500779

[31] Yiğiterol F., Güllü H. H. & Yildiz D. E. (2018) Inflence of Si_3N_4 layer on the electrical properties of Au/n-4H SiC diodes Bull. Mater. Sci. 41(3), 66-9, https://doi.org/10.1007/s12034-018-1586-2

CHAPTER
4

AN UPPER QUANTITATIVE ESTIMATE ON A CIRCULAR ANNALUS FOR COMPLEX MODIFIED PHILLIPS OPERATORS

Esma YILDIZ ÖZKAN[1]

Introduction

Bernstein (Bernstein, 1912) found the proof of the Weierstrass approximation theorem based law of large numbers for a sequence of Bernoulli trials. He constructed, for any continuous function $f \in C[0,1]$, a sequence of polynomials

$$B_n(f;x) = \sum_{k=0}^{n} f\left(\frac{k}{n}\right)\binom{n}{k} x^k (1-x)^{n-k}, n = 1,2,\ldots$$

and proved that the sequence converges to f for $n \to \infty$ uniformly with respect to $x \in [0,1]$. These polynomials called Bernstein polynomials, possess many remarkable properties. They have been studied intensively.

Many well-known operators preserve the test functions e_0 and e_1, such as Bernstein polynomials (Bernstein, 1912), Meyer-König and Zeller operators (Meyer-König&Zeller, 1960), Baskakov operators (Baskakov, 1957) etc. Observe that these operators do not preserve the test function e_2. King (King, 2003) proposed a non-trivial sequence of linear positive operators by modifying the Bernstein polynomials, which approximate each continuous function on [0,1] and preserving the test function e_0 and e_2, and it is proved that the operators proposed by King have better rate of convergence on the interval [0,1/3] over the Bernstein polynomials. Later, a lot of authors studied similar problem for certain operators.

Phillips (Phillips, 1954) defined the following operators

$$P_n(f;x) = n\sum_{\vartheta=1}^{\infty} s_{n,\vartheta}(x)\int_0^{\infty} s_{n,\vartheta-1}(t)\, f(t)dt + e^{-nx}f(0),$$

where $x \in [0,+\infty)$ and

$$s_{n,\vartheta}(x) = exp(-nx)\frac{(nx)^{\vartheta}}{\vartheta!}.$$

May (May, 1977) studied some direct and inverse results on these operators. In (Zhou, 1985), the approximation properties of Phillips operators were studied. In (Gupta&Agrawal, 1989; Gupta&Sahai, 1993; Agrawal&Gupta, 1990), the linear combinations and the iterative combination of Phillips operators were obtained respectively. In (Gal&Gupta, 2014), the complex Phillips opera-

---

[1]

tors were defined. In (Gupta&Tachev, 2014), the approximation by linear combinations of complex Phillips operators was studied in compact disks.

Let $(r_n(x))$ be the sequence of real-valued continuous functions defined on $[0,+\infty)$, with $0<(r_n(x))<1$. Gupta (Gupta, 2010) defined the following modified Phillips operators:

$$P_n(f;r_n(x)) = n\sum_{\vartheta=1}^{\infty} s_{n,\vartheta}(r_n(x))\int_0^{\infty} s_{n,\vartheta-1}(t)\,f(t)dt + e^{-nr_n(x)}f(0),$$

where

$$f\in C_\gamma[0,+\infty) := \{f\in C[0,\infty): f(t)=O(t^\gamma), \gamma>0\}$$

the norm $\|.\|_\gamma$ on $C_\gamma[0,+\infty)$ is defined as

$$\|f\|_\gamma = sup_{x\in[0,+\infty)}|f(t)|t^{-\gamma}.$$

Replacing $r_n(x)$ by $r_n^*(x)$, which are defined by

$$r_n^*(x) = -\frac{1}{n}+\sqrt{\frac{1}{n^2}+x^2},$$

the following positive linear operators were obtained

$$\tilde{P}_n(f;r_n^*(x)) = n\sum_{\vartheta=1}^{\infty} s_{n,\vartheta}(r_n^*(x))\int_0^{\infty} s_{n,\vartheta-1}(t)\,f(t)dt + e^{-nr_n^*(x)}f(0),$$

where $f\in C_\gamma[0,+\infty)$ and $x\in[0,+\infty)$. The operators $\tilde{P}_n$ are King type (King, 2003) operators preserving the test functions e_0 and e_2. Also, It can be seen that $\tilde{P}_n$ maps $C_B[0,+\infty)$the space of all bounded and continuous functions on [0,+∞), into itself.

Gupta gave the rate of convergence for the modified Phillips operators and showed the error estimation for the modified Phillips operator is better than the original Phillips operators.

Definition of Complex Modified Phillips Operators

Definition 1. We define the following complex modified Phillips operators:

$$\tilde{L}_n(f)(z) = n\sum_{\vartheta=1}^{\infty} s_{n,\vartheta}(r_n^*(z))\int_0^{\infty} s_{n,\vartheta-1}(t)\,f(t)dt + e^{-nr_n^*(z)}f(0),$$

where $f:\overline{D}_R\cup(\mathrm{R},+\infty)\to\mathbb{C}$ is continuous function,

$$s_{n,\vartheta}(z) = exp(-nz)\frac{(nz)^\vartheta}{\vartheta!}$$

and

$r_n^*(z) = -\frac{1}{n} + \sqrt{\frac{1}{n^2} + z^2}$.

These complex modified Phillips operators are linear.

Auxilary Results

We can give the following auxiliary results in order to get our main theorem:

Lemma 1. We have the following equalities for the operators $\tilde{L}_n$:

(i) $\tilde{L}_n(e_0)(z) = 1$

(ii) $\tilde{L}_n(e_1)(z) = -\frac{1}{n} + \sqrt{\frac{1}{n^2} + z^2}$

(iii) $\tilde{L}_n(e_2)(z) = z^2$

(iv) $\tilde{L}_n(\varphi_z)(z) = -z - \frac{1}{n} + \sqrt{\frac{1}{n^2} + z^2}$

(v) $\tilde{L}_n(\varphi_z^2)(z) = 2z\left(z + \frac{1}{n} - \sqrt{\frac{1}{n^2} + z^2}\right)$,

where $e_i(t) = t^i$ for $i = 0,1,2$ are the test functions and $\varphi_z(t) = t - z$ and $\varphi_z^2(t) = (t - z)^2$ are central moments.

Proof. Replacing x by z, in Lemma 2.1 and Lemma 2.2 in (Gupta, 2010), the proof of the lemma can be obtained easily.

Lemma 2. Suppose that $f\colon \overline{D}_R \cup (\mathrm{R}, +\infty) \to \mathbb{C}$ is analytic in D_R i.e. $f(z) = \sum_{k=0}^{\infty} c_k z^k$ for all $z \in D_R$, and bounded on $[\mathrm{R}, +\infty)$. For all $z \in D_R$, we have

$\tilde{L}_n(f)(z) = \sum_{k=0}^{\infty} c_k \tilde{L}_n(e_k)(z)$.

Proof. For any $m \in \mathbb{N}$ and $r < R$, let us define

$f_m(z) = \sum_{j=0}^{m} c_j z^j$ if $|z| \leq r$ and $f_m(x) = f(x)$ if $x \in (r, +\infty)$.

It is clear that $|f_m(z)| \leq \sum_{j=0}^{m} |c_j| r^j \coloneqq C_r$ for all $|z| \leq r$. From the hypothesis on f, f is continuous on $[r, R]$ and bounded on $[\mathrm{R}, +\infty)$. Then it is clear that for any $m \in \mathbb{N}$ it follows $|f_m(x)| = |f(x)| \leq C_{r,R}$ for all $x \in [r, R]$ and $|f_m(x)| = |f(x)| \leq C_R$ for all $x \in [\mathrm{R}, +\infty)$ and for any $m \in \mathbb{N}$. There exist $C > 0$ with $C \geq max\{C_r, C_{r,R}, C_R\}$ that $|f_m(x)| \leq C$ for all $x \in [0, +\infty)$.

This implies that for each fixed $m, n \in \mathbb{N}$ and $z \in D_R$,

$$\left|\tilde{L}_n(f_m)(z)\right| \leq C\left|e^{-nr_n^*(z)}\right|\left(\sum_{j=1}^{\infty} \frac{(n|r_n^*(z)|)^j}{j!} n \int_0^{\infty} e^{-nt} \frac{n^{j-1}}{(j-1)!} t^{j-1} dt \; + |C'|\right)$$

$$= C\left|e^{-nr_n^*(z)}\right|(1 + |C'|) \sum_{j=1}^{\infty} \frac{(n|r_n^*(z)|)^j}{j!} < +\infty,$$

since by the ratio criteria the last series is convergent, so $\tilde{L}_n(f_m)(z)$ is well defined.

Denoting

$f_{m,k}(z) = c_k e_k(z)$ if $|z| \leq r$ and $f_{m,k}(x) = \frac{f(x)}{m+1}$ if $x \in (r, +\infty)$,

it is clear that each $f_{m,k}$ is bounded on $[0,+\infty)$ and that $f_m(z) = \sum_{k=0}^{m} f_{m,k}(z)$. Since from the linearity of $\tilde{L}_n$ we have

$$\tilde{L}_n(f_m)(z) = \sum_{k=0}^{m} c_k \, \tilde{L}_n(e_k)(z)$$

for all $|z| \leq r$.

It suffices to prove that

$$\lim_{m\to\infty} \tilde{L}_n(f_m)(z) = \tilde{L}_n(f)(z)$$

for any fixed $n\in\mathbb{N}$ and $|z| \leq r$. But this proof is immediate from

$$\lim_{m\to\infty} \|f_m - f\|_r = 0,$$

from the inequality

$$\|f_m - f\|_{B[0,+\infty)} \leq \|f_m - f\|_r$$

and from the inequality

$$\left|\tilde{L}_n(f_m)(z) - \tilde{L}_n(f)(z)\right| \leq \left|e^{-nr_n^*(z)}\right| e^{-n|r_n^*(z)|} \|f_m - f\|_{B[0,\infty)} + \left|e^{-nr_n^*(z)}\right| |f_m(0) - f(0)|$$

valid for all $|z| \leq r$.

Here $\|.\|_{B[0,+\infty)}$ denotes the uniform norm on $B[0,+\infty)$ the space of all complex-valued bounded functions on [0,+∞).

Lemma 3. Denoting $e_k(z) = z^k$ and $H_{n,k}(z) = \tilde{L}_n(e_k)(z)$, we have the following recurrence formula:

$$H_{n,k+1}(z) = \frac{r_n^*(z)}{n[r_n^*(z)]'} H'_{n,k}(z) + \frac{k + nr_n^*(z)}{n} H_{n,k}(z),$$

for $k = 1,2, \ldots$.

Proof. Using

$$s'_{n,\vartheta}\big(r_n^*(z)\big) = [r_n^*(z)]' \left\{-n + \frac{\vartheta}{r_n^*(z)}\right\} s_{n,\vartheta}\big(r_n^*(z)\big)$$

and

$$z s'_{n,\vartheta}(z) = (\vartheta - nz) s_{n,\vartheta}(z),$$

we have

$$\frac{r_n^*(z)}{[r_n^*(z)]'} H'_{n,k}(z) = n \sum_{\vartheta=1}^{\infty} \frac{r_n^*(z)}{[r_n^*(z)]'} s'_{n,\vartheta}\big(r_n^*(z)\big) \int_0^{\infty} s_{n,\vartheta-1}(t)\, t^k dt$$

$$= n \sum_{\vartheta=1}^{\infty} \{-nr_n^*(z) + \vartheta\} s_{n,\vartheta}\big(r_n^*(z)\big) \int_0^{\infty} s_{n,\vartheta-1}(t)\, t^k dt$$

$$= n \sum_{\vartheta=1}^{\infty} s_{n,\vartheta}\big(r_n^*(z)\big) \int_0^{\infty} \{-nr_n^*(z) + 1 + \vartheta - 1 - nt + nt\} s_{n,\vartheta-1}(t)\, t^k dt$$

$$= n \sum_{\vartheta=1}^{\infty} s_{n,\vartheta}\big(r_n^*(z)\big) \int_0^{\infty} s'_{n,\vartheta-1}(t)\, t^{k+1} dt + \big(1 - nr_n^*(z)\big) H_{n,k}(z) + nH_{n,k+1}(z)$$

Thus integrating by parts the last integral, we obtain

$$\frac{r_n^*(z)}{[r_n^*(z)]'} H'_{n,k}(z) = -\big(k + nr_n^*(z)\big) H_{n,k}(z) + nH_{n,k+1}(z),$$

this completes the proof of the recurrence relation.

Remark 1. The above recurrence formula works in the circular annulus $\{z \in \mathbb{C}: 0 < |z| < R\}$ for $0 < R < +\infty$, since $1/[r_n^*(z)]'$is defined for $z \neq 0$, so we need to use the circular annulus

$$D_{R,n} := \left\{z \in \mathbb{C}: \frac{1}{n} < |z| < R\right\}$$

for $0 < R < +\infty$, in order to get an upper estimate.

By A_R we mean the class of all functions satisfying: $f: \overline{D}_R \cup (\mathrm{R}, +\infty) \to \mathbb{C}$ is continuous function, bounded on $[\mathrm{R}, +\infty)$. and analytic in D_R i.e. $f(z) = \sum_{k=0}^{\infty} c_k z^k$ for all $z \in D_R$.

Main Result

Now, we can give the following upper quantitative estimate of the operators $\tilde{L}_n$.

Theorem 1. Let $f \in A_R, 1 \leq r < R < +\infty$ and suppose that there exists $M > 0$ and $A \in \left(\frac{1}{R}, 1\right)$, with the property that $|c_k| \leq M \frac{A^k}{(5k)!}$, for all $k = 0,1, \dots$. Let $1 \leq r < \frac{1}{A}$. Then there exists $n_0 \in \mathbb{N}$ such that for all $z \in \overline{D}_{r,n}$ and $n \in \mathbb{N}$ with $n > n_0$ we have

$$\left|\tilde{L}_n(f)(z) - f(z)\right| \leq \frac{C_{r,A}}{n},$$

where

$$C_{r,A} = \frac{M}{r} \sum_{k=2}^{\infty} (rA)^k < +\infty.$$

Proof. Using the recurrence formula in Lemma 3, we can write

$$\begin{aligned} H_{n,k}(z) - z^k = {} & \frac{1}{n}\left(-\frac{\sqrt{\frac{1}{n^2} + z^2}}{nz} + \frac{1}{n^2 z} + z\right) \\ & \times \left[H_{n,k-1}(z) - z^{k-1}\right]' \\ & + \left(\frac{k-2}{n} + \sqrt{\frac{1}{n^2} + z^2}\right)\left[H_{n,k-1}(z) - z^{k-1}\right] \\ & + \frac{1}{n}\left(-\frac{\sqrt{\frac{1}{n^2}+z^2}}{nz} + \frac{1}{n^2 z} + z\right)(k-1)z^{k-2} \\ & + \frac{1}{n}(k-2)z^{k-1} + \left(\sqrt{\frac{1}{n^2} + z^2} - z\right) z^{k-1} \end{aligned}$$

For $|z| \leq r$, taking absolute value, we obtain

$$\begin{aligned} \left|H_{n,k}(z) - z^k\right| \leq {} & \frac{1}{n}\left|-\frac{\sqrt{\frac{1}{n^2} + z^2}}{nz} + \frac{1}{n^2 z} + z\right| \\ & \times \left|\left[H_{n,k-1}(z) - z^{k-1}\right]'\right| \end{aligned}$$

$$+\left|\frac{k-2}{n}+\sqrt{\frac{1}{n^2}+z^2}\right|\left|H_{n,k-1}(z)-z^{k-1}\right|$$
$$+\frac{1}{n}\left|-\frac{\sqrt{\frac{1}{n^2}+z^2}}{nz}+\frac{1}{n^2z}+z\right|(k-1)|z|^{k-2}$$
$$+\frac{1}{n}(k-2)|z|^{k-1}$$
$$+\left|\sqrt{\frac{1}{n^2}+z^2}-z\right||z|^{k-1}$$

On the other hand, the sequence $\left\{\sqrt{\frac{1}{n^2}+z^2}\right\}$is uniformly convergent to z for all $z\in\overline{D}_{r,n}$, so there exists $n_0\in\mathbb{N}$ such that for all $n>n_0$ and $z\in\overline{D}_{r,n}$

$$\left|\sqrt{\frac{1}{n^2}+z^2}-z\right|\leq\frac{1}{n}$$

For all $z\in\overline{D}_{r,n}$, by using triangle inequality, we have

$$\left|-\frac{\sqrt{\frac{1}{n^2}+z^2}}{nz}+\frac{1}{n^2z}+z\right|\leq\frac{\sqrt{\frac{1}{n^2}+|z|^2}}{n|z|}+\frac{1}{n^2|z|}+|z|$$
$$\leq\frac{\frac{1}{n}+|z|}{n|z|}+\frac{1}{n^2|z|}+|z|$$
$$\leq 3+r$$

and

$$\left|\frac{k-2}{n}+\sqrt{\frac{1}{n^2}+z^2}\right|\leq\frac{k-1}{n}+r,$$

which implies for all $z\in\overline{D}_{r,n}$,

$$\left|H_{n,k}(z)-z^k\right|\leq\frac{1}{n}(3+r)\left|\left[H_{n,k-1}(z)-z^{k-1}\right]'\right|$$
$$+\left(\frac{k-1}{n}+r\right)\left|H_{n,k-1}(z)-z^{k-1}\right|$$
$$+\frac{5(k-1)r^{k-1}}{n} \qquad (1)$$

Now, for $1\leq r<R$, if we denote the norm $\|.\|_r$ in $C(\overline{D}_r)$where $\overline{D}_r=\{z\in\mathbb{C}\colon|z|\leq r\}$, then by a linear transformation, the Bernstein's inequalty in the closed unit disks becomes

$$|P_k'(z)|\leq\frac{k}{r}\|P_k\|_r$$

for all $|z|\leq r$, where $P_k(z)$is a polynomial of degree $\leq k$. Thus from (1), we have

$$\left\|H_{n,k}-e_k\right\|_r\leq\frac{1}{n}(3+r)\frac{k-1}{r}\left\|H_{n,k-1}-e_{k-1}\right\|_r$$

$$+\left(\frac{k-1}{n}+r\right)\left\|H_{n,k-1}-e_{k-1}\right\|_r+\frac{5(k-1)r^{k-1}}{n},$$

which implies the relation

$$\left\|H_{n,k}-e_k\right\|_r\leq\left(\frac{5(k-1)}{n}+r\right)\left\|H_{n,k-1}-e_{k-1}\right\|_r+\frac{5(k-1)r^{k-1}}{n}.$$

In whats follows we prove the result by mathematical induction with respect to k (with $n\geq 1$ supposed to be fixed arbitrarily), that this recurence implies

$$\left\|H_{n,k}-e_k\right\|_r\leq\frac{(5k)!r^{k-1}}{n} \tag{2}$$

for all $k=1,2,\ldots$ and $n=1,2\ldots.$

Indeed while for $k=1$, we get

$$\left\|H_{n,1}-e_1\right\|_r\leq\frac{2}{n}<\frac{5!}{n}$$

and for $k=2$, it is clear that

$$\left\|H_{n,2}-e_2\right\|_r=0<\frac{10!\,r}{n}.$$

Suppose that it is true for k, the above recurrence relation implies that

$$\begin{aligned}\left\|H_{n,k+1}-e_{k+1}\right\|_r&\leq\left[\left(\frac{5k}{n}+r\right)\frac{(5k)!}{n}+\frac{5kr}{n}\right]r^{k-1}\\&\leq\left[\frac{(5k+1)!r}{n}+\frac{5kr}{n}\right]r^{k-1}\\&\leq\frac{(5k+5)!r^k}{n}\end{aligned}$$

In conclusion, the estimate in (2) is valid.

Now, from the hypothesis on f, it follows that $\tilde{L}_n(f)(z)$ is analytic in D_R. Thus by Lemma 2, we can write

$$\tilde{L}_n(f)(z)=\sum_{k=0}^{\infty}c_k\,\tilde{L}_n(e_k)(z)$$

for all $z\in D_R$, which from the hypothesis on c_k immediately implies for all $z\in\overline{D}_{R,n}$

$$\begin{aligned}\left|\tilde{L}_n(f)(z)-f(z)\right|&\leq\sum_{k=1}^{\infty}|c_k|\left|\tilde{L}_n(e_k)(z)-e_k(z)\right|\\&\leq\sum_{k=1}^{\infty}M\frac{A^k}{(5k)!}\frac{(5k)!}{n}r^{k-1}\\&=\frac{1}{n}\frac{M}{r}\sum_{k=1}^{\infty}(rA)^k.\end{aligned}$$

Choosing

$$C_{r,A}=\frac{M}{r}\sum_{k=2}^{\infty}(rA)^k<+\infty$$

for $1\leq r<\frac{1}{A}$, the desired result is obtained.

Consequence and an Open Problem

Theorem 1 has an important role in order to obtain the total convergence of the complex modified Phillips operators. After calculating a lower quantitative estimate for the complex modified Phillips operators, it can be given a total convergence theorem, which is an open problem for the reader.

References

1. Agrawal, P.N.&Gupta, V. (1990). On the iterative combination of Phillips operators. *Bull. Inst. Math. Acad. Sinica*, 18(4): 361-368.

2. Baskakov, V.A. (1957) An example of a sequence of linear positive operators in the space of continuous function (Russian). *Dokl. Akad. Nauk SSSR*. 113:249-251.

3. Bernstein, S.N. (1912). Démonstration du théorème de Weierstrassfondée sur le calcul de probabilités, *Commmun. Soc. Math. Kharkow*, 13(2):1-2.

4. Gal, S. G.&Gupta, V. (2014). *Approximation by Complex Durrmeyer Type Operators in Compact Disks:Mathematics Without Boundaries*, New York.

5. Gupta, V. (2010). A Note on Modified Phillips Operators,.*Southeast Asian Bull. Math.*, 34: 847-851.

6. Gupta, V.&Agrawal, P.N. (1989). Linear combinations of Phillips operators. *J. Indian Acad. Math.*, 11(2): 106-114.

7. Gupta, V.&Sahai, A. (1993). On the linear combinations of Phillips operators. *Soochow J. Math.*, 19(3): 313-323.

8. Gupta, V.&Tachev, G. (2014). Approximation by linear combinations of complex Phillips operators in compact disks. *Results Math.*,66(1-2): 265-272. https://doi.org/10.1007/s00025-014-0377-3.

9. King, J.P. (2003). Positive linear operators which preserve x2. *Acta Math. Hungar.*, 99: 203-208.

10. May, C.P. (1977). On Phillips operators. *J. Approx. Theory*, 20: 315-332.

11. Meyer-König, W.&Zeller, K. (1960). Bernsteinsche potenzereihen, *Studia Math.*, 19:89-94.

12. Phillips, R.S. (1954). An inversion formula for Laplace transforms and semi-groups of linear operators. *Ann. Math.*, 59: 325-356.

13. Zhou, X.L. (1985). Approximation properties of the Phillips operator. *(Chinese) J. Hangzhou Univ. Natur. Sci. Ed.*, 12(3): 300-306.

CHAPTER
5

INVESTİGATİON OF SİNTERİNG TEMPERATURE ON THE STRUCTURAL, ELECTRİCAL AND MAGNETİC PROPERTİES OF MGB$_2$ SAMPLES

Sait Barış GÜNER[1]

INTRODUCTION

In 1911, three years after first liquefying helium, Kamerlingh Onnes unexpectedly found while investigating the resistivity of mercury at low temperatures that at ~4.2 K the resistivity of his sample suddenly dropped dramatically (Onnes, 1911). Further investigation showed that the resistance had actually dropped to zero and not just to a very low value. This marked the first observation of superconductivity in a material which had been cooled to below a certain temperature, its transition temperature (T_c). A superconducting material has two important properties which make its performance separate from all other materials. These properties are both electromagnetic in nature, and a superconductor's unique response to electric and magnetic fields is what determines its use in various applications such as field trapping and magnetic levitation. With the discovery of superconductivity, many scientists focus on this field. Various natural elements and simple compounds exhibit superconductivity at extremely low temperatures, including lead at Nb3Sn at 18.3 K (Matthias et al., 1954) and niobium at 9.2 K (Roberts, 1976). Later, in 1987, Maw-Kuen Wu and Ching-wu Chu replaced the lanthanum in LaBCO with yttrium, i.e., synthesising a Y-Ba-Cu-O (YBCO) superconductor, which raised Tc to 93 K (Wu et al., 1987). During the late 1980s and the early 1990s, superconducting materials with even higher Tc than YBCO were discovered, such as Bi-Sr-Ca-Cu-O at 108 K (Takagi et al., 1988), Tl-Ba-Ca-Cu-O at 127 K (Hazen et al., 1988) and Hg-Ba-Ca-Cu-O at 153 K under 30 GPa (Chu et al., 1993).

The more recent discovery of MgB_2 superconductors has broadened further the family of superconducting materials. In the 21st century, Prof. J. Akimitsu found that MgB_2 which is a metallic superconductor has a high critical temperature of 40 K, for the first time (Buzea & Yamashita, 2001). As a result, several researchers have made up the interest because of its many advantages. One of the most important advantages is the cheap price of magnesium and boron powders and a simple fabrication process (Ulgen & Belenli, 2017a). Unlike other superconductors, MgB_2 has a lower anisotropy, larger coherence length, clean grain boundaries to current flow, and therefore is a good candidate for practical applications (Ulgen et al., 2019; Ağıl et al., 2017a).

Furthermore, in place of processing at the temperature of 4.2K with liquid helium like Nb3Ge metal based superconductor, the MgB_2 which can work liquid

---

[1] Corresponding Author Department of Physics, Faculty of Arts and Sciences, Recep Tayyip Erdogan University, 53100, Rize, Turkey

hydrogen (20 K) which is cheaper and easier applicable for practical applications (Kajikawa et al., 2009; Muralidhar et al.,2015). On the other hand, the bulk MgB_2 magnets are quite similar to those of melt-textured GdBaCuO and more gorgeous for trapped field magnets particularly in nuclear magnetic resonance (NMR) and magnetic resonance imaging (MRI), fault current limiters, non-contact bearings for liquid pumping, and for magnetic shielding screens (Vinod et al., 2007; Perini et al. 2009; Ağıl et al., 2017b). All these applications need high critical current density and good quality, large-sized bulk materials.

Recent research reports have demonstrated that the sintering parameters have a noteworthy inspiration on the structure, electrical and magnetic properties of MgB_2 superconducting material (Ulgen & Belenli, 2017b; Kobayashi et al., 2015). Controlling the micro-structural properties by changing the optimum processing parameters is found to be effective in enhancing Jc values of MgB_2 (Ulgen & Belenli, 2017c; Yamamoto et al.,2014).

Recent reports have showed that the magnetic levitation force and trapped field studies of MgB_2 increase bulk significantly. Several groups have already reported the magnetic levitation measurements of bulk MgB_2 materials. Magnetic levitation force abilities of MgB_2 bulk superconductors about 17 N/g at around 16 K was first demonstrated by Yanmaz et al. (Yanmaz et al., 2010). Savaskan et al. was reported high magnetic levitation force value of nearly 18.60 N at 24 K for MgB_2 malic acid added bulk MgB_2 superconductors with a diameter of 18 mm (Savaşkan et al., 2014). On the other hand, quite a few researchers have already studied the trapped field capatiy of bulk MgB_2 materials. High trapped field values of around 1.5 T at 20 K and 2.3 T at 6 K for MgB_2 sample with a diameter of 28 mm and 11 mm height was showed by Viznichenko et al. (Viznichenko et al., 2003). The maximum trapped magnetic field of MgB_2 bulk was measured around 5.4 T at 12 K (Fuchs et al., 2013). Subsequently, Yamamoto et al. studied that a MgB_2 bulk of 20 mm diameter and 5 mm thickness fabricated with a simple sintering technique showed trapped field of around 1.2 T at 20 K (Yamamoto et al., 2010).

High critical current density (J_c) and good homogeneity are necessary for high magnetic trapped field and magnetic levitation force performance. Superconducting properties of a bulk material depend on the processing conditions, like the synthesis temperature, holding time, annealing atmosphere, additives etc. In order to achieve the high trapped field in MgB_2, optimization of the synthesis temperature is essential. As a result bulk MgB_2 samples of 20 mm diameter and 7 mm thickness, sintered at 805 °C for 3h, demonstrated a trapped field of 1.51 T at T = 20 K (Muralidhar et al., 2013). In this paper, we study the optimization of the sintering temperature to improve the critical current density of large bulk MgB_2 bulks prepared by a simple solid state reaction method and studied the X-ray diffraction, scanning electron microscopy (SEM), superconducting transition temperature, and magnetic levitation force. One of the most important parameters depending on magnetic levitation force is the critical current density. To enhance the highest magnetic levitation force capacity of the bulk MgB_2 at 30 K, we fixed the initial ratio of Mg:B to 1:2, holding time was constant for 3 h, annealing atmosphere was pure argon and the synthesis temperature was varied for sintering different temperatures of 700, 750, 775, 800 and 850 °C. After the optimum sintering temperature of bulk MgB$_2$ was determined, the holding times at 775 °C were changed from 1 hour to 5 hours.

MATERIALS AND METHODS

Nano boron (purity 95 %+) and magnesium (purity 98 %+) powders supplied by Pavezyum Company Turkey were used to fabricate the Bulk MgB$_2$ samples. The powders of Mg metal and amorphous B powder were mixed in a nominal ratio of Mg: B = 1: 2 with 1.5 g. Different contents of magnesium powder were added into each sample and mixed in a glass of bottle for 10 min. The mixture was grounded for 20 min using an agate mortar and pressed into a pellet form with a diameter of 18 mm under 10 ton pressures. These pellets were placed in a chromium tube which is in the center of cylindrical furnace. After that, the tube was vacuumed and pellets were annealed at 700, 750, 775, 800 and 850 °C for 3 h and 775 °C for 1 h. During the thermal process, high purity argon gas was supplied into tube. The heating and cooling rates were used 5 °C/min.

The microstructures of MgB$_2$ bulks were investigated by scanning electron microscope (SEM) JEOL JSM 6610 with an accelerating voltage of 20 kV in the secondary electron image mode on small specimens cut from the MgB$_2$ samples. The phase constituents of samples were analyzed the X-ray diffraction by using a Rikagu D/Max III C diffractometer with a step size of 0.02 in the range of 20-70° using Cu Kα (λ= 1.5406 Å) target.

The specimen with dimensions about 1.5 x 1.5 x 1 mm3 were cut from different temperatures sintered MgB$_2$ samples and magnetization versus applied magnetic field measurement (M-H) and magnetization versus temperature (M-T) was carried out using Quantum Design PPMS-9 T system. Magnetic hysteresises (M-H) of the specimens were measured at 30 K, up to the magnetic field of ±9 T with a sweep rate of 50 Oe/s. The critical current density, J$_c$, was calculated from the width of magnetization hysteresis loops based on the extended Bean model (Bean, 1964).

Vertical levitation force (F$_z$) versus vertical distance (z) measurement between the bulk MgB$_2$ samples of thickness 3.20 mm and a diameter of 19.60 mm (after thermal process) and the cylindrical NdFeB permanent magnet (18 mm in diameter and 10 mm in thickness) with the surface magnetic flux of 0.5 T were performed using the Magnetic Levitation Force Measurement System (MLFMS), designed by Şükrü Çelik and financially supported by The Scientific and Technological Research Council of Turkey (TUBITAK). This system contains modular parts such as a stainless steel vacuum chamber, close cycle cryostat, high vacuum pumping system (rotary pump and turbo molecular pump), precision three dimensional movable axes, three axis loadcell, and electronic part and software. The vertical magnetic levitation force (F$_z$) measurements were performed under zero field cooling regime (ZFC) in CH 51.5 mm (CH represent the cooling height of the sample), while the F$_z$ measurements (in other words, the F$_z$ in field cooling regime (FC)) were carried out under FC regime at the temperatures 30 K. The centers of the all samples were located axially over the center of PM before cooling process. Unlike the ZFC regime, for force measurements in FC regime, firstly the samples were cooled in CH of 1.5 mm, then the samples were moved away vertically to 51.5 mm distance from PM and subsequently returned to the initial position of 1.5mm (Çelik, 2015).

RESULTS AND DISCUSSION

Fig. 1 shows the X-ray diffraction patterns of the MgB_2 samples fabricated sintering process at 700, 750, 775, 800 and 850 °C for 3h. It can be said that main phase (*101*) of the MgB_2 matrix can be obtained from the XRD analyses of samples sintered for 3 h at 700, 750, 775, 800 and 850 °C. XRD analysis revealed that a little amount of MgO impurity decreases. Besides main phase, a significant amount of unreacted magnesium and MgB_4 phases also observed at 700 °C for 3h because of the non-reaction between magnesium and nano-boron at this sintering temperature. Further, a lot of Mg is still present as primary phase in the Mg+2B samples sintered at lower temperatures around 700 °C, defining the MgB_2 phase formation at the solid-solid reaction stage (Ma & Liu, 2012).

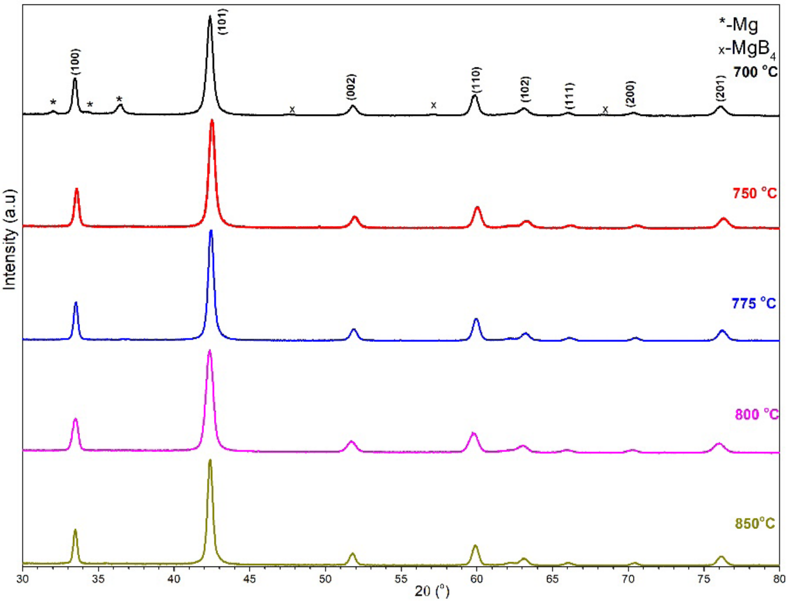

Figure 1. X-ray diffraction patterns of MgB_2 samples sintered at 700–850 °C.

Figure 2 indicates the temperature dependence of normalized magnetic moment of the MgB_2 samples fabricated sintering process at 700, 750, 775, 800 and 850 °C in argon atmosphere. According to the inset of Figure 2, all samples have an onset superconducting transition in the range 38.4 K - 39.3 K. The high Tc of 39.3 K observed sample sintered at 850 °C. Figure 3 shows the compare of different holding times from 1 hour to 5 hours at 775 °C. The onset temperature increases from 1 h to 3 h while it decreases from 3 h to 5 h (inset; Figure 3). As observed by Figure 2 and Figure 3, sample sintered at 775 °C for 3h has the sharpest superconducting transition width and one of the highest onset temperatures. The high Tc and the sharp superconducting transition show that MgB_2 samples reveal good crystallinity and homogeneity. The observed superconducting transition temperatures are similar to the recently reported bulk MgB_2 material fabricated with a solid-state reaction method (Naito et al., 2012; Muralidhar et al., 2014). These results suggest that superconducting transition temperature in the superconducting matrix in bulk MgB_2 materials is not so sensitive to sintering time and holding time.

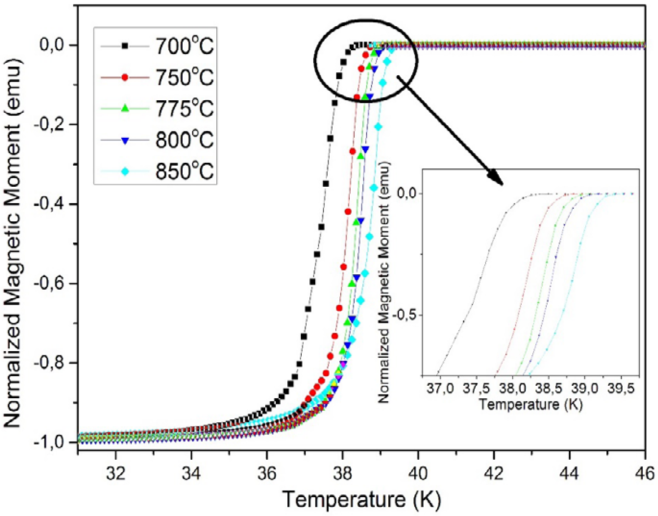

Figure 2. Temperature dependence of normalized magnetic moment for MgB_2 samples fabricated sintering technique at 700, 750, 775, 800 and 850 °C for 3 h in argon atmosphere.

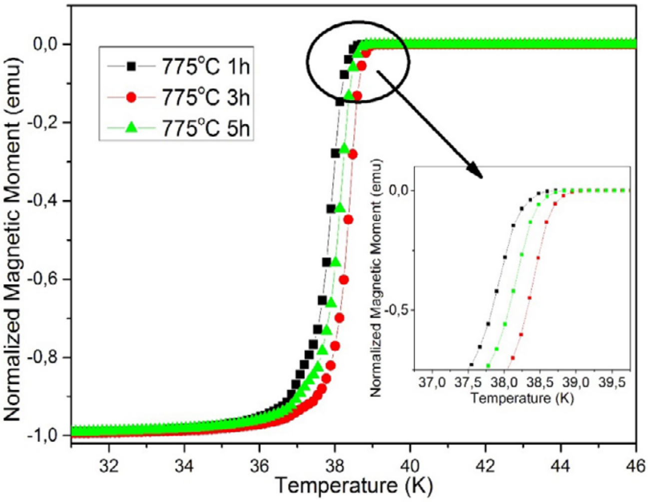

Figure 3. Temperature dependence of normalized magnetic moment for MgB_2 samples fabricated sintering technique for 1 hour, 3 and 5 hours at 775 °C in argon atmosphere.

Figure 4 shows the critical current behavior of the bulk MgB_2 material at 30 K, sintered at 700, 750, 775, 800 and 850 °C for 3 h in argon atmosphere. It was remarkable that the critical current density increased with increasing the sintering temperature from 700 °C to 775 °C. As sintering temperatures increase from 775 °C to 850 °C, the critical current density of them decreases significantly. Note that the highest critical current density of 69 kA/cm2 and 23 kA/cm2 at 20 K, in self-field and 1T was recorded for the sample sintered for 3h at 775 °C. The critical current density variables obviously show that the low temperature synthesis with optimum temperature can be the most promising and effective technique to achieve high critical current density in sintered bulk MgB_2 material (Kobayashi et al., 2015). These variables again obviously reveal that optimum sintering temperature is essential to take the high critical current density in bulk MgB_2 material.

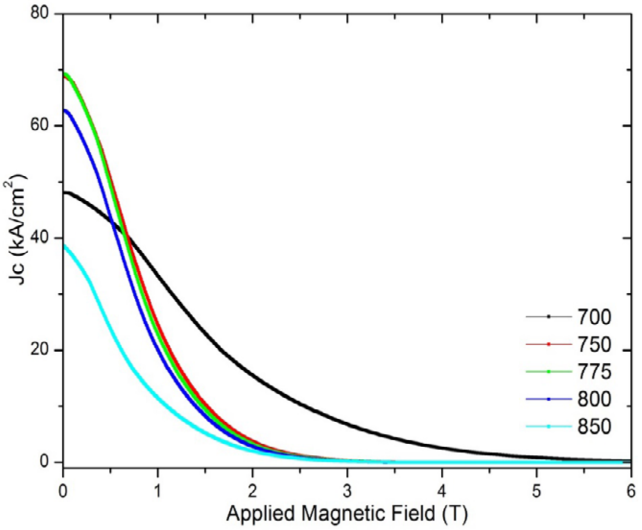

Figure 4. Applied magnetic field versus critical current densities at T = 30 K for MgB_2 samples sintered at 700–850 °C in Ar atmosphere.

The vertical levitation force (Fz) of MgB_2 sintered at 700, 750, 775, 800 and 850 °C for 3 h samples and PM under ZFC and FC regimes at the temperature of 30 K was shown in Figure 5 and Figure 6, respectively. When the Fz values under ZFC regime compared to FC regime, it can be observed that FC regime can take a smaller levitation value but a good stability owing to the trapped flux and this is consistent with the literature (Wu et al., 2013; Kurabayashi et al., 2010; Savaskan et al., 2015). As can be showed from the inset graphs in Figure 5 and Figure 6, the maximum repulsive and attractive force values increase from 6.39 N to 8.23 N and the minus value of 2.38 N to 3.01 N, respectively, when sintering temperature rises from 700 to 775 °C. It is inferred that the optimum sintering temperature for strong maximum levitation force is 775 °C at 30 K. There is a relation with the levitation force between a PM and a superconductor is related with the magnetic moment of the superconductor and magnetic field gradient of PM, given as $Fz=m(dH/dz)$ where m is the magnetic moment of a superconductor and dH/dz is the external field gradient obtained by the PM. Total magnetic moment of the superconductor is determined as; $m = (JcAr)V$, where A is a sample geometry constant, r is the radius of a shielding current loop and V is the sample volume (Ozturk et al., 2017). These relations point out that to perform a higher magnetic levitation force value the higher r, Jc and dH/dz are necessary. There is a good agreement between the critical current density results and magnetic levitation force measurements at 30 K.

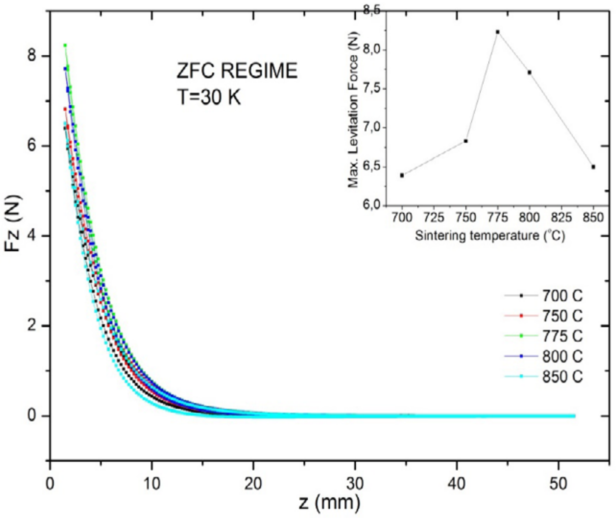

Figure 5. Levitation force of MgB_2 sintered at 700, 750, 775, 800 and 850 °C for 3 h versus distances curves of under ZFC regime at 30 K. Inset indicates maximum levitation force values versus the sintering temperatures.

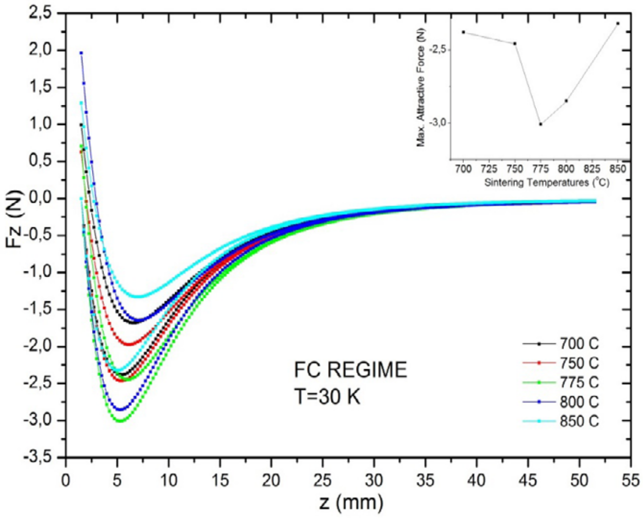

Figure 6. Levitation force of MgB_2 sintered at 700, 750, 775, 800 and 850 °C for 3 h versus distances curves of under FC regime at 30 K. Inset shows maximum attractive force values versus the sintering temperatures.

Figure 7 shows high resolution compositional SEM images of polished cross sections of the MgB_2 material sintered at 700, 775 and 850 °C for 3 h in Ar atmosphere. As analyzed Figure 7, MgO grain observes especially MgB_2 material sintered at 700 °C and then the amount of the MgO decreases with increasing sintering temperature with 775 °C. SEM image taken at a high magnification clearly indicated the grain structure. Some grains grew large as the sintering temperature increased from 775 to 850 °C. As can be seen in the SEM images; the amount of porosity decreases with increasing sintering temperature from 700 to 775 °C. However, the sintering temperature rises from 775 to 850 °C with increasing the amount of porosity. This problem can be originated lack of magnesium evaporation. The presence of such porosities will reduce the superconducting current carrying area, and therefore the overall Jc in the MgB_2 material (Liu et al., 2003). XRD analysis also supported the result of the SEM analysis that the MgO formation takes place at high sintering temperatures. About the grain size and phase purity, sintering at 775 °C appears to be optimum for the fabrication of MgB_2 bulk samples with good quality. Additional, the analysis of SEM images is directly related with the results of critical current density and magnetic levitation force.

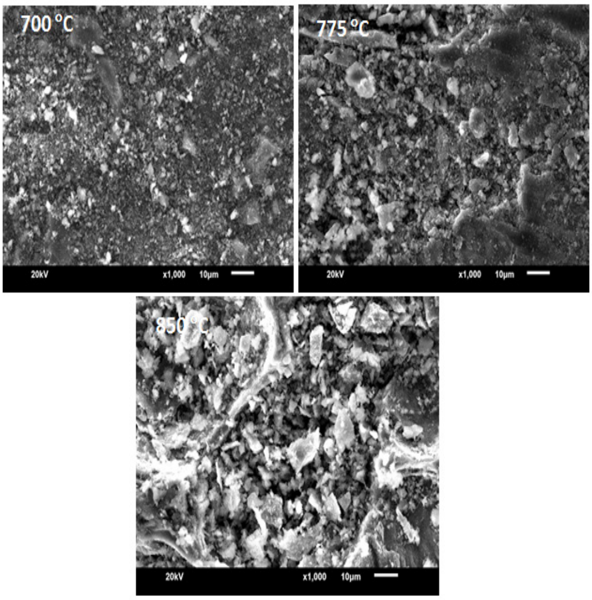

Figure 7. SEM pictures of MgB_2 samples sintered at 700, 775 and 850 °C for 3 hours.

CONCLUSIONS

Bulk MgB_2 samples were prepared via solid-state reaction at various sintering temperatures of 700, 750, 775, 800 and 850 °C for 3 h °C in pure Ar atmosphere. X-ray diffraction, magnetization and scanning electron microscopy (SEM) analyses indicated that single-phase and homogenous MgB_2 bulks are produced by sintering at 775 °C, and therefore the highest critical current density (Jc) was recorded in that sample. The zero-field Jc value reached as 69 kA/cm2. The magnetic levitation force measurement results showed that processing temperature is the fundamental way to improving magnetic levitation force values. Bulk MgB_2 sample of 19.60 mm diameter and 3.20 mm thickness, sintered at 775 °C, showed a levitaton force of 8.23 at T = 30 K. Magnetic levitation force at around liquid hydrogen temperature (<30 K) illustrate that the bulk MgB_2 magnets have high potential for a variety of high field technological applications.

ACKNOWLEDGEMENTS

This research was supported by Recep Tayyip Erdoğan University Scientific Research Projects Coordination Department. Project Number: 918. All the magnetic levitation force measurements were carried out in the MLFMS made by the project of TUBİTAK Project No: 110T622 (Patent application number is 2013/13638).

REFERENCES

1. H. Kamerlingh Onnes, Akad. van Wetenschappen (Amsterdam), 14: 818, 1911.
2. B. T. Matthias, T. H. Geballe, S. Geller, and E. Corenzwit, "Superconductivity of Nb3Sn", Phys. Rev., 95-6, (1954) 1435.
3. B. W. Roberts, "Survey of superconductive materials and critical evaluation of selected properties", J. Phys. Chem. Ref. Data, 5:581-821, 1976.
4. M. K. Wu, J. R. Ashburn, C. J. Torng, P. H. Hor, R. L. Meng, L. Gao, Z. J. Huang, Y. Q. Wang, and C. W. Chu, "Superconductivity at 93 K in a new mixed-phase Yb-Ba-Cu-O compound system at ambient pressure", Phys. Rev. Lett., 58(9):908-910, 1987.
5. H. Takagi, H. Eisaki, S. Uchida, A. Maeda, S. Tajima, K. Uchinokura, and S. Tanaka, "Transport and optical studies of single crystals of the 80 K Bi-Sr-Ca-Cu-O superconductor", Nature, 332:236-238, 1988.
6. R. M. Hazen, L. W. Finger, R. J. Angel, C. T. Prewitt, N. L. Ross, C. G. Hadidiacos, P. J. Heaney, D. R. Veblen, Z. Z. Sheng, A. El Ali, and A. M. Hermann, "100 K superconducting phases in the Tl-Ca-Ba-Cu-O system", Phys. Rev. Lett., 60-(16) 1657-1660, 1988.
7. C. W. Chu, L. Gao, F. Chen, Z. J. Huang, R. L. Meng, and Y. Y. Xue, "Superconductivity above 150 K in HgBa2Ca2Cu3O8+δ at high pressures", Nature, 365:323-325, 1993.
8. C. Buzea and T. Yamashita, "Review of the superconducting properties of MgB_2", Supercond. Sci. Technol., 14:R115-R146, 2001.
9. A. T. Ulgen, I. Belenli, "Time-Dependent Diffusion Coefficient of Fe in MgB_2 Superconductors", Journal of Superconductivity and Novel Magnetism, 30(12):3367–3375, 2017.
10. A. T. Ulgen, F. Karaboğa, M. Karakaya, R. Podila, A. M. Raoe, I. Belenli, "Improved transport properties of MgB_2 superconducting round wires via minute addition of gold nanoparticle", Ceramics International,45(1):1031-1036, 2019.

11. H. Ağıl, E. Aksu, A. Gencer, "Role of Aniline Addition in Structural and Superconducting Properties of MgB_2 Bulk Superconductor", J. Supercond. Nov. Magn., 30:2735–2740, 2017a.

12. K. Kajikawa, T. Nakamura, "Proposal of a fully superconducting motor for liquid hydrogen pump with MgB_2 wire", IEEE Trans. Appl. Supercond., 19:1669-1672, 2009.

13. M. Muralidhar, K. Nozaki, H. Kobayashi, X.L. Zeng, A. Koblischka-Veneva, M.R. Koblischka, K. Inoue, M. Murakami, "Optimization of sintering conditions in bulk MgB_2 material for improvement of critical current density", J. Alloys Compd., 649:833-842, 2015.

14. K. Vinod, R.G. Abhilash Kumar, U. Syamaprasad, "Prospects for MgB_2 superconductors for magnet application", Supercond. Sci. Technol., 20:R1-R13, 2007.

15. E. Perini, G. Ginuchi, "Field cooling of a MgB_2 cylinder around a permanent magnet stack: prototype for superconductive magnetic bearing", Supercond. Sci. Technol., 22:045021, 2009.

16. H. Ağıl, E. Aksu, S. Akturk, A. Gencer, "The Effects of Structural, Thermal, and Magnetic Properties of Hexylbenzene-Doped MgB_2 Superconductor", J. Supercond Nov Magn., 30:1727–1736, 2017b.

17. A. T. Ulgen, I. Belenli, "The Effect of Fe Diffusion on Some Physical and Superconducting Properties of MgB_2", Journal of Superconductivity and Novel Magnetism, 30(4):1089–1095, 2017b.

18. H. Kobayashi, M. Muralidhar, M R. Koblischka, K. Inoue, M. Murakami, "Improvement in the Performance of Bulk MgB_2 Material through Optimization of Sintering Process", Physics Procedia, 65:73 – 76, 2015.

19. A. T. Ulgen, I. Belenli, "Sintering time dependence of iron diffusion in MgB_2 and its effect on superconducting properties", AIP Conference Proceedings 1815:040008, 2017c.

20. A. Yamamoto, A. Ishihara, M. Tomita, and K. Kishio, "Permanent magnet with MgB_2 bulk superconductor", Appl. Phys. Lett., 105:032601, 2014.

21. E. Yanmaz, K. Ozturk, C.E.J. Dancer, M. Basoğlu, S. Celik, C.R.M. Grovenor, "Levitation force at different temperatures and superconducting properties of nano-structured MgB_2 superconductors", J. Alloys Compd., 492:48-51, 2010.

22. Savaşkan, E.T, Koparan, Ş. Çelik, K. Öztürk, E. Yanmaz, "Investigation on the Levitation Force Behaviour of Malic Acid Added Bulk MgB_2 Superconductors", Physica C, 502:63-69, 2014.

23. R.V. Viznichenko, A.A. Kordyuk, G. Fuchs, K. Nenkov, K.H. Müller, T.A. Prikhna, W. Gawalek, "Temperature dependence of the trapped magnetic field in MgB_2 bulk superconductors", Appl. Phys. Lett., 83:4360–4362, 2003.

24. G. Fuchs, W. Haßler, K. Nenkov, J. Scheiter, O. Perner, A. Handstein, T. Kanai, L. Schultz, B. Holzapfel, “High trapped fields in bulk MgB_2 prepared by hot-pressing of ball-milled precursor powder”, Supercond. Sci. Tech., 26:122002, 2013.
25. A. Yamamoto, H. Yumoto, J. Shimoyama, K. Kishio, A. Ishihara, M. Tomita, Abstract of 23rd Int. Symp. on Supercond., Tsukuba, Japan, 1–3:219, 2010.
26. M. Muralidhar, A. Ishihara, K. Suzuki, Y. Fukumoto, Y. Yamamoto, M. Tomita, “Optimization of the fabrication process for high trapped field MgB_2 bulks”, Physica C, 494:85–88, 2013.
27. P. Bean, “Magnetization of high-field superconductors”, Rev Mod Phys., 36:31-39, 1964.
28. S. Çelik, “Design of magnetic levitation force measurement system at any low temperatures from 20 K to room temperature”, J Alloys Compd., 662:546-556, 2015.
29. Z. Ma and Y. Liu, Sintering of Ceramics – New Emerging Techniques, INTECH, 21:469-484, 2012.
30. T. Naito, T. Sasaki, H. Fujishiro, “Trapped magnetic field and vortex pinning properties of MgB_2 superconducting bulk fabricated by a capsule method”, Supercond. Sci. Technol., 25:095012, 2012.
31. M. Muralidhar, K. Inoue, M.R. Koblischka, M. Tomita, M. Murakami, “Optimization of processing conditions towards high trapped fields in MgB_2 bulks”, J. Alloys Compd., 608:102–109, 2014.
32. X. Wu, K. Xu, Y. Cao, S. Hu, P. Zuo, G. Li, “Modeling of hysteretic behavior of the levitation force between superconductor and permanent magnet”, Physica C, 486:17–22, 2013.
33. H. Kurabayashi, S. Horikoshi, A. Suzuki, M. Ikea, A. Wongsatanawarid, H. Seki, S. Akiyama, M. Hiragushi, M. Murakami, “Interaction between ring permanent magnets and bulk Dy-Ba-Cu-O superconductors”, Physica C, 470:1853–1855, 2010.
34. B. Savaskan, E. Taylan Koparan, S.B. Güner, S. Çelik, K. Öztürk, E. Yanmaz, “Effect of $C_4H_6O_5$ Adding on the Critical Current Density and Lateral Levitation Force of Bulk MgB_2”, J. Low Temp. Phys., 181:38–48, 2015.
35. K. Ozturk, C.E.J. Dancer, B. Savaskan, C. Aksoy, B. Guner, P. Badica, G. Aldica, S. Celik, “The investigation on the regional nanoparticle Ag doping into $MgTi_{0.06}B_2$ bulk for improvement the magnetic levitation force and the bulk critical current”, Journal of Alloys and Compounds, 724:427-434, 2017.
36. C.F. Liu, G. Yan, S.J. Du, W. Xi, Y. Feng, P.X. Zhang, X.Z. Wu, L. Zhou, “Effect of heat-treatment temperatures on density and porosity in MgB_2 superconductor”, Physica C, 386:603–606, 2003.

CHAPTER
6

DETERMINATION OF MELTING TEMPERATURES IN ORTHORHOMBIC STRUCTURES FROM ELASTIC CONSTANTS

Tahsin ÖZER

INTRODUCTION

The raw materials in nature are converted into usable material by passing various processes. The material has been important since the existence of humanity. Nowadays it is still important. In order to maintain technological developments, the material is a critical element [1].

The elastic properties of the solids are associated with physical properties such as heat capacity, melting point, bonding between atoms, and Debye temperature [2]. Elastic constants of the solid; gives interesting information about the mechanical and dynamic properties of the material [3]. The experimental determination of these quantities under high pressure is difficult due to the difficulty of the experimental conditions [4]. Because of this relationship is very important parameters for technological applications [5]. Because of the relationship between the melting temperature and the elastic constants, the melting temperature of the material can be calculated from the elastic constants. The use of empirical relations in determining the melting temperature will prevent the time and material consumption used in experimental studies. Melting temperature with empirical relations; It can be easily and quickly predicted.

The success of a project is largely dependent on the materials used in the project. The selection of conscious material suitable for the project is possible by knowing the properties of the materials. Experimental studies can be carried out to determine the properties of materials and theoretical studies can be carried out. In theoretical studies, the computing power of computers is widely used. The subject of the theoretical studies can be experimental studies, yet the features that have not yet been subject to an experimental study can even create the properties of the non-synthesized materials. Computer calculations help reduce research costs while helping to understand physical phenomena [6]. Much faster results can be obtained by using empirical relations.

Numerous studies have been conducted in the literature to determine the melting temperatures of materials [7,8]. There are empirical equations for determining the melting temperatures of cubic, hexagonal and tetragonal materials [9, 10]. In the literature, we could not find any empirical relationship to determine the melting temperatures of orthorhombic structures. In this sense; equation for determination of melting temperatures from elastic constants of orthorhombic structures was first proposed with this study. As statistical the coefficient of determination of the proposed equation is quite high with a rate of 99.9%.

MATERIALS AND METHODS

Too many variables can come together and influence another variable. These variables can also affect each other among themselves. For example, if there is a linear relationship between the descriptor variable x_1 and the descriptor variable x_2, this causes the problem of multiple internal relations. These two explanatory variables do not need to be present in the model at the same time. One of the variables is enough in the model [11]. Scatter diagrams are plotted to easily visualize the relationship between variables. Scatter diagrams show the relationship and the shape of the relationship.

The equation, which determines the functional form of the relationship between variables, is called the regression equation. In cases where a variable is used, a single regression analysis is performed. Regression analysis using multiple independent variables is called “multiple regression analysis”.

X_i; variable or independent variables, e_i; the error term and Y; indicate the response variable or dependent variable, the most common multiple regression equation;

$$Y= a_0 + a_1X_1 + a_2X_2 + \dots + a_kX_k + e_i \qquad (1)$$

In the equation, a0; when $X_i = 0$, Y is the value. a1, a2, ak, is the regression coefficient, and X is the unit of change in 1 unit of its own unit. The term ei; error represents, in a way, the argument that is not included in the model. There are different methods [12?] and software to solve the regression equations. SPSS and the MINITAB software used in this study are some of them. To see the strength and direction of the relationship between two quantitative variables visually, a scattering diagram is drawn [12]. If there is no relationship between variables, regression anal cannot be applied. The scatter diagram drawn for this study is shown in Figure 2. Examples of scattering diagrams showing the shape and direction of the relationship are given in the following Figure 1.

It is not correct to estimate for an X which other than the change interval values used for calculating the regression coefficient of the regression equation. If an X value outside this range is used for estimation from the regression equation, the estimation may be inaccurate [12].

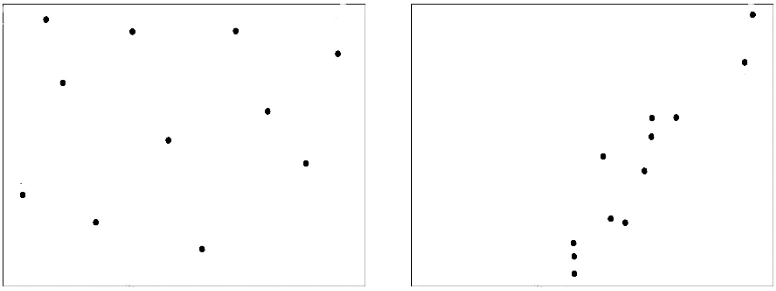

(a) (b)

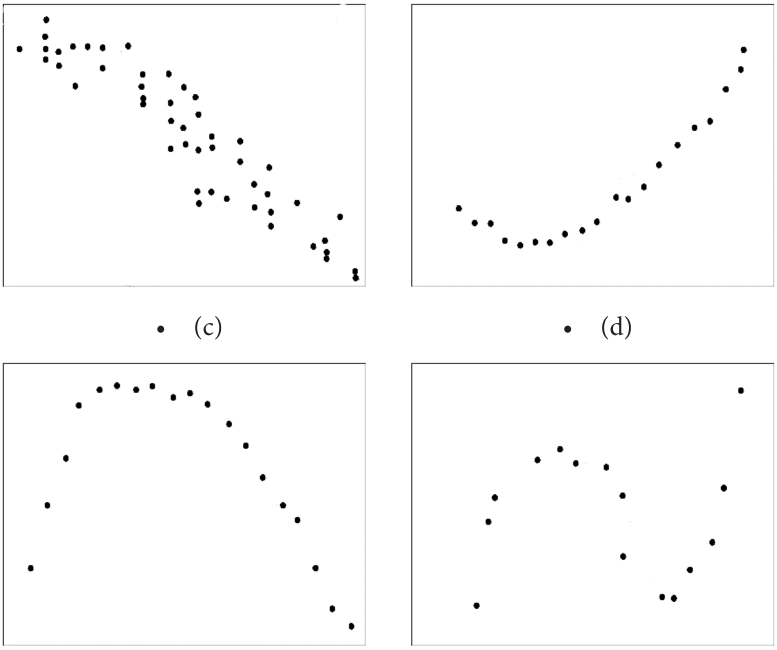

• (c) • (d)

(e) (f)

Figure 1: Scattering diagrams, (a) There is no relationship between variables, (b) There is a positive linear relationship between variables, (c) There is a negative linear relationship between variables, (d) The relationship between variables is parabolic, (e) The relationship between the variables is parabolic in a negative direction, (f) The relationship between variables is curvilinear.

After the regression coefficients are calculated and the regression estimation model is established, coefficients of determination (R^2 and corrected R^2) are calculated. The value of R^2 indicates "X_i" variables explain the what percentage explains of the total change in "Y". In regression models with the same number of explanatory variables, R^2 uses the corrected R^2 value in regression models with a different number of explanatory variables [11]. The coefficients of determination take the values $0 \leq R^2 \leq 1$.

The R^2 value is. "0" indicates that the variability in the dependent variable cannot be explained by the argument. "1" indicates that the variability in the dependent variable is fully explained by the argument. [12].

RESULTS AND DISCUSSION

For regression analysis, there should be a relationship between variables. This relationship can be seen visually from the scattering diagrams. The melting temperatures and elastic constants supplied from the literature review are given in Table 1. The scattering diagram for orthorhombic structures using the values given in Table 1 is given in Figure 2.

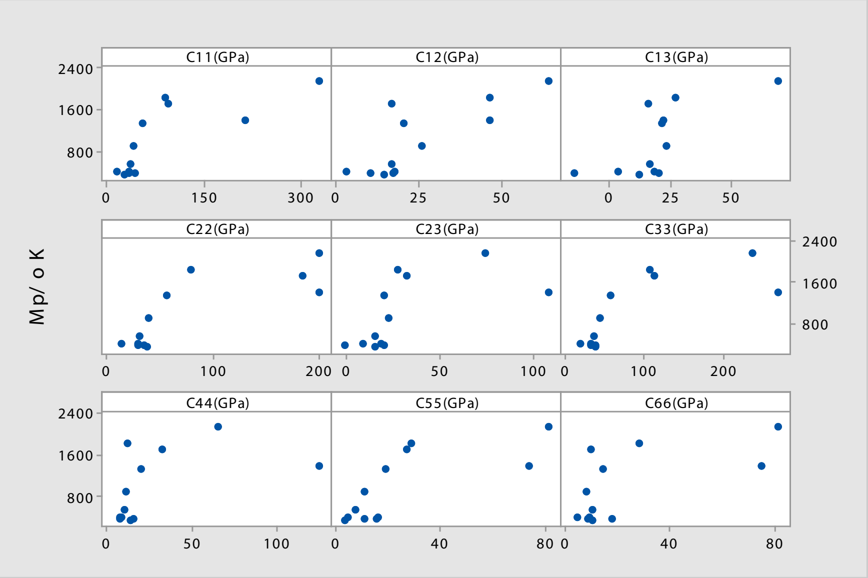

Figure 2: Scattering diagram for orthorhombic structures.

From scatter diagrams; it can be seen there is a clear relationship between variables. For orthorhombic structures, variance and regression analyzes were performed with MINITAB 17 [13] software on the data shown in Table 1. As a result of the analysis, the regression coefficient was statistically significant and the coefficient of determination of the model was 99.9%. According to this result 99.9% of the variability in the melting temperature of an orthorhombic material can be explained by the elastic constants C_{11}, C_{12}, C_{13}, C_{22}, C_{23}, C_{33}, C_{44}, C_{55} and C_{66}, 0.1% cannot be explained by these constants. M_p, regression equation to indicate the melting temperature in Kelvin (K) degrees,

$$M_p = 246.3 - 3.10\, C_{11}\,(\text{GPa}) + 7.72\, C_{12}\,(\text{GPa}) + 55.92\, C_{13}\,(\text{GPa}) - 20.90\, C_{22}\,(\text{GPa}) - 122.17\, C_{23}\,(\text{GPa}) + 58.99\, C_{33}\,(\text{GPa}) + 58.16\, C4_4\,(\text{GPa}) + 42.07\, C_{55}\,(\text{GPa}) - 114.9\, C_{66}\,(\text{GPa}) \qquad (2)$$

From this equation; It is observed that C_{12}, C_{13}, C_{33}, C_{44} and C_{55} increase the melting temperature, C_{11}, C_{22}, C_{23} and C_{66} decrease the melting temperature.

The comparison of the melting temperatures obtained using the proposed equation in this study is done in Table 1. As can be seen from Table 1, the values calculated using Equation (2) are quite consistent with experimental values. The maximum difference between the calculated values and the experimental values given in Table 1 is 9.7%, the smallest difference is 0.02% and average 2.78%.

Table 1: Comparison of melting temperatures for orthorhombic structures (C_{ij} in GPa, Melting point (M_p) in K)

Formula	**Mp**	**C11**	**C12**	**C13**	**C22**	**C23**	**C33**	**C44**	**C55**	**C66**	**From eq(2)**	**Dif.**
$(NH_4)_2SO_4$ [8]	553	36.07	16.51	15.8	29.81	14.56	35.34	10.25	7.17	9.74	607.01	9.77
$BaSO_4$ [8]	1853	89.41	46.14	26.91	78.42	26.76	105.48	11.9	28.74	27.78	1853.43	0.02
$CaSO_4$ [8]	1733	93.82	16.5	15.2	184.5	31.73	111.8	32.47	26.53	9.26	1736.00	0.17
Mg_2SiO_4 [8]	2170	328.48	63.9	68.8	199.8	73.8	235.3	65.15	81.2	80.88	2169.09	0.04
$MgSO_4.7H_2O$ [8]	423	32.5	17.4	18.2	28.8	18.2	31.5	7.8	15.6	9	406.23	3.96
$KNaC4H_4O_6.4H_2O$ [8]	343	25.5	14.1	11.6	38.1	14.6	37.1	13.4	3.2	9.8	321.28	6.33
K_2SO_4 [8]	1342	53.57	19.99	20.95	56.53	19.9	55.23	19.5	18.79	14.24	1339.88	0.16
$Sr(CHO_2)_2.2H_2O$ [8]	373	43.91	10.37	-14.9	34.84	-1.4	37.46	15.38	10.75	17.24	375.55	0.68
S_8 [7]	421	14.22	2.99	3.14	12.68	7.95	18.3	8.27	4.28	4.37	403.07	4.26
Tl_2SO_4 [8]	905	41.06	25.73	22.88	38.85	21.74	42.68	11.25	10.68	7.51	887.56	1.93
U [8]	1408	214.86	46.22	21.76	199.83	107.64	267.63	124.79	73.79	74.54	1412.03	0.29
$ZnSO_4.7H_2O$ [8]	373	33.2	17.2	20	29.3	19.8	32	7.8	15.3	8.3	394.56	5.78
Min.	343	14.22	2.99	-14.90	12.68	-1.40	18.30	7.80	3.20	4.37	321.28	0.02
Max.	2170	328.48	63.90	68.80	199.83	107.64	267.63	124.79	81.20	80.88	2169.09	9.77
Mean.	**991**	**83.88**	**24.75**	**19.20**	**77.62**	**29.61**	**84.15**	**27.33**	**24.67**	**22.72**	**992.14**	**2.78**

CONCLUSION

The melting temperatures and elastic constants of orthorhombic structures were obtained from the literature review. In order to know the relationship between these data and the variables visually, scatter diagrams were drawn. There was a relationship between melting temperature and elastic constants. Variance and regression analysis were performed by using MINITAB 17 software. As a result of these analyzes, regression equation which predicts melting temperatures from elastic constants was proposed with a 99.9% coefficient of determination in the 95% confidence interval for orthorhombic structures. The melting temperatures estimated using the proposed equation in this study; compared with experimental data.

REFERENCES

1. Erdoğan, D., "Malzeme bilgisi", Ankara Üniversitesi Ziraat Fakültesi yayını, Ankara, 2007(Turkish).
2. Liu, C., Chen, X., Ji, G. "First-principles investigations on structural, elastic and electronic properties of SnO$_2$ under pressure", Computational Materials Science, 50, 1571-1577, 2011.
3. Çabuk, S. "Ab initio volume-dependent elastic and lattice dynamics properties of KTaO$_3$", Phys. Status Solidi B, 247, 1, 93–97, 2010.
4. Özer, T., Çabuk, S., Karataşlı, M. "Investigation of Mechanical Properties of SnO2 Crystals in CaCl$_2$ Type Structure", AKU J. Sci.Eng.17, 021101 (399-405), 2017.
5. Ozer, T., Cabuk, S. "First-principles study of the structural, elastic and electronic properties of SbXI (X=S, Se, Te) crystals", Journal of Molecular Modeling 24: 66, 2018.
6. Ozer, T. "Investigation of Structural, Dynamic and Thermodynamic Properties of SbXI (X = S, Se, Te) Compounds with Ab Initio Method", PhD thesis, Çukurova University Institute of Natural and Applied Sciences Department of Physics, 148 Pages, Adana, 2016 (Turkish).
7. Madelung, O. "Semiconductors: Data Handbook" 3rd edition, Springer, Germany, 2004.
8. Rumble, J.R. (Editor in chief). "CRC handbook chemistry and physics" 98 th edition, Boca Raton, USA, 2017-2018.
9. Özer, T. "Determination of melting temperature", 4 th International Congress on Multidisciplinary Studies 18th -19 th October 2018, Kyrenia-TRNC, 2018.
10. Fine, M.E., Brown, L.D., Marcus, H.L. "Elastic constant versus melting temperature in metals", Scripta Metalurgica, 18, 951-956, 1984.
11. Erol, H. "SPSS Paket program ile istatiksel very analizi", Nobel kitabevi, Adana, 2010 (Turkish).
12. Gürsakal, N. "Çıkarımsal istatistik", 6. Baskı, DORA, 2014 (Turkish).
13. MINITAB 17. Available: http://www.minitab.com/en-us/ products/minitab/